Cracking in Hot-dip Galvanized Welded Joints of Steel Platform Structures

by

Christopher T. DiGiovanni

A thesis submitted in partial fulfillment of the requirements for the degree of

Master of Science

in

Welding Engineering

Department of Chemical and Materials Engineering
University of Alberta

Abstract

In a recent construction project, a platform structure made up of 350W and 300W steel underwent a double dip galvanizing process. Prior to the galvanizing process, the platform was fabricated to completion, which included numerous welds throughout the design. After galvanizing, cracks were found originating in the welds and propagating into the base material. To the steel designer, this posed a new and curious problem. Previously, similar structures had undergone the same processing with no cracking.

This research project began by investigating the metallurgy and microstructure of the base material, the welds, and of the crack sites. Two key features that were noted were the thicker and inclusion-rich grain boundaries in the base material, and the cracking appeared with little or no deformation of the grains. In addition, the fracture surfaces were studied at high magnification levels and showed features of brittle fracture, which is uncharacteristic of the 350W and 300W steels used. Studies were carried out to asses the material's susceptibility to both hydrogen embrittlement and temper embrittlement, both of which are known to potentially occur during galvanizing.

Tension test samples were sectioned from the base material and were charged with hydrogen. During the tension testing, the samples charged with hydrogen did not show any different behavior from the regular samples. All the fracture surfaces were ductile and did not match the surfaces from the galvanizing cracks. Furthermore, hardness levels were too low to be deemed susceptible to hydrogen cracking according to the values seen in literature. Similarly, samples were sectioned from the base material and notched for temper embrittlement testing. The samples were heated to the galvanizing temperature and then fractured. The samples broke suddenly and showed little signs of ductile fracture and, more significantly, had a fracture surface matching the original cracks. To support the notion of temper embrittlement, material chemistry testing found high levels of phosphorus. Phosphorus is a key culprit in temper embrittlement, and given the elevated temperature and stress of the double dip process, it would have been able to diffuse to the grain boundaries causing brittle grain boundary separation. Finally, to quantify the thermal stresses induced from galvanizing, a three dimensional finite element analysis model was created to simulate the double dip process. The model found relatively high stresses but not enough to reach the yield point without an embrittlement factor present.

Preface

The material presented in this thesis are parts of the research project under the supervision of Dr. Leijun Li, which was funded by Waiward Steel LLP and MITACS. This thesis is the study that was completed to provide Waiward Steel with a full scale examination and explanation for the cracking that occurred in one of their construction projects. The study and results were condensed into a research article submitted to the Engineering Failure Analysis Journal.

Chapter 3 of this thesis includes a 3-dimensional model of the steel structure that was studied. The design of the structure is the intellectual property of Waiward Steel LLP.

Chapters 4 and 5 of this thesis involve original and unique test experiments developed by the author. The tests were developed to thoroughly and empirically test the material for embrittlement susceptibility, in accordance to the material and equipment that was available. All testing was done on samples provided by Waiward Steel LLP.

Acknowledgement

I would like to thank Dr. Leijun Li for giving me the amazing opportunity to be a part of his research group in physical and welding metallurgy. His love and enthusiasm for metallurgy has been truly inspiring throughout my degree and has driven me to reach further in my academic and professional life. On the numerous occasions I showed up unannounced in Dr. Li's office I was always greeted with a smile, and my questions were always greeted with patience. I would also like to thank Dr. Robert Driver for introducing myself and Dr. Li to the project my thesis is based on, and making me feel welcome in the Steel Centre's group. His wisdom, insight and understanding have been irreplaceable throughout my graduate studies. As the next stage of my career is ahead, I hope to keep in touch and a maintain a friendship with both Dr. Li and Dr. Driver in the years to come.

I would like to recognize MITACS for their funding to make this research project possible. Without their contribution the research and student stipend costs would not have been met. Along with MITACS I would like to thank Waiward Steel LLP and Logan Callele for giving us the opportunity to work on this project, and for their contribution to the project's funding. They also provided all the samples used in this thesis and gave valuable insight into the project's background.

I would like to thank everyone involved in Dr. Li's research group including Jason Wang, Rangasayee Kannan, Neil Anderson, and Daniel Yang. Their patience in teaching me to use the metallography equipment and operating the SEM with me in the evenings can not be over stated. Their warm reception when I first moved to Alberta from Ontario was welcoming and kind. Attending conferences with them has easily been the highlights of my degree, not only for the memories and laughs we shared, but also because it was an opportunity to see them present their work with admirable passion. I would also like to include Victoria Buffan and Riley Quinton of The Steel Centre group in the thanks of my colleagues. They were both always a reliable source for guidance using Abaqus, and our rants and stories of frustration over the software were always appreciated.

My family has supported me throughout my degree and has made my life insurmountably better. They have always supported my decisions and encouraged me to follow my dreams and desires. Their unconditional love, patience, and care have helped me throughout my entire life and words cannot express my gratitude.

Contents

List of Figures

List of Tables

1. Introduction

1.1. Introduction

For almost two hundred and fifty years galvanization has been used as the primary procedure to protect steels from the corrosive atmosphere [1, 2]. The process involves applying a protective and thin layer of zinc to a thicker base material, typically steel. Without the protective zinc layer, the steel would form rust (a type of iron oxide) in the open air atmosphere [3]. However, the corrosion of zinc occurs significantly slower which makes it a good protective layer and lengthens the product life of the covered base material. In addition to its anti-corrosive properties, zinc will also act as a sacrificial anode. This advantage is what makes galvanizing superior to something like painting, since exposed areas do not need immediate touch ups, because the sacrificial zinc anode will protect the base material [4].

There are three different types of processes used to apply the zinc layer to the base material. The first and most widely used process is hot-dip galvanizing. This is the process of submerging the base material in a bath of molten zinc. However, the surface must cleaned entirely and rid of any oxides to ensure a strong metallic bond is formed [5, 6]. This is also the most cost-effective process. The next type is pre-galvanizing. Pre-galvanizing is similar to hot-dip galvanizing, except it occurs at the steel mill, where the rolled metal sheets are put through the same cleaning process followed by a bath of molten zinc. This process allows for a more uniform coat, but if the sheets are cut for fabrication, large sections of the base material can be exposed to the atmosphere [3]. The last process is electrogalvanizing. Unlike the previous two processes, electrogalvanizing does not rely on a molten zinc bath, but rather applies the zinc layer using an electric current in electrolyte solution to apply zinc ions. This process gives the greatest degree of control on the coating thickness and gives a much more uniform coat [3].

In the case of larger steel assemblies, a double dip process may be used. This is a variant to hot-dip galvanizing, in which the structure is too large to be fully submerged in the zinc bath. Instead, half of the structure is dipped and coated with zinc, followed by the remaining half. A concern when using a double dip procedure is the large temperature gradient across the structure, since half the structure will be exposed to the ambient air while the other half is submerged in the molten bath. The thermal stresses induced could be considerable depending

on the design of the structure.

In a construction project in the Edmonton area, a platform structure was going into service outdoors and, since it was fabricated from 350W and 300W structural steel, required corrosion protection. However, due to the size of the structure and its fabrication prior to galvanizing, it also required a double dip procedure. The structure was made up of various wide-flanged beams, T-beams and C-channels (the C-channels were the 300W components). The beams were welded using a metal core arc welding process for the flanges and a flux core arc welding process for the webs of the beams. After fabrication, the platform had exterior dimensions of approximately 3m x 7m.

The steel platforms underwent the typical procedure for double dip galvanizing. They were first processed with the caustic cleaning to remove any contaminants such as oil, grease, paint or dirt. Next, it was cleaned in the pickling bath to remove any oxides or rust from the base material's surface. Finally, before being submerged in the molten zinc bath, the structure underwent fluxing which removes any oxides still present and deposits a protective layer to shield the structure before being put into the zinc bath.

Upon inspection after galvanizing, numerous cracks were found initiating in the welded joints and propagating into the base material. Cracking was found across several different platforms and in different types of joints. To the steel structure designers this was an unexpected complication to the project. Previous projects with similar designs that had also undergone a double dip galvanizing procedure did not experience any cracking. The welds were inspected after fabrication and no signs of a pre-existing crack or defect were found. A third party consulting company was brought in to investigate the cracking, but strong conclusive results were not found.

The galvanizing company however did not claim this was an outlandish result. Cracking during hot dip galvanizing, especially double dip galvanizing, is a known phenomenon. Several types of embrittlement can occur during galvanizing, including liquid metal embrittlement (LME), hydrogen embrittlement, and temper embrittlement [7–10]. Also, the double dip process can lead to thermal stresses potentially exceeding the yield strength under certain designs. Exploring each embrittlement type and understanding what makes a material susceptible is key to understanding the cracking situation studied, and cracking during galvanizing as a whole.

1.2. Thesis Objective

The objective of this thesis is to assist the galvanizing and steel structures industry by uncovering the cause of cracking in this incident, and demonstrating the methods used. The thesis aims to show what factors of the galvanizing process and material made the structure susceptible to cracking, which can be carried forward by industry in future projects.

1.3. Thesis Outline

Each chapter of the thesis is a study of a different aspect of interest, including its own background, experimental procedures, and conclusions. Each chapter builds on the knowledge base which is used in the succeeding chapters, until an overall and final conclusion can be drawn.

Chapter 2 focuses on the metallurgy of the steel, along with the fractography of the original cracks and lab-produced cracks. This study establishes a base of information from which the experimental direction can be drawn.

Chapter 3 shows the creation of the finite element model to simulate the double dip process. The stress and temperature readings from the model indicate that an embrittlement factor must have been present since the thermal stress did not exceed the yield point. They also show a stress distribution matching the crack shape indicating the double dip process was the driving force for cracking.

Chapter 4 outlines a study on hydrogen cracking susceptibility by measuring hardness and more explicitly by mechanically testing and fracturing samples charged with hydrogen. The low hardness and absence of any difference in the charged samples implies the material is not susceptible to hydrogen cracking in this case and can be eliminated as a possibility.

Finally in Chapter 5 temper embrittlement susceptibility is tested by heating samples to the galvanizing temperature and fracturing them, along with studying the material chemistry. The results show features similar to those found in the original cracks.

2. Metallography, Microstructure, and Fractography

2.1. Introduction

Metallography is the study of the structure and distribution of components, at a microscopic level. Metallography is typically carried out using microscopy techniques along with appropriate sample preparation. For example, using a different etchant on a metal can show different phase structures of interest. Metallography serves as the cornerstone in understanding material properties, and can even be used to predict material behaviors and characteristics [11].

Surface preparation for a metallographic study is critical. If the surface is not prepared properly, or is prepared poorly, the features of the microstructure will not be clear and furthermore will not look presentable. The sample surfaces are typically prepared mechanically, using a finer and finer abrasive until the surface is completely flat. The surface is then burned with a select etchant to show the features of interest. Metallography is carried out using an optical microscope or an electron microscope. An optical microscope is more desirable for low level magnification images, and the natural colour of the sample can also still be seen. However, for more detailed and higher level magnification images a scanning electron microscope (SEM) is the optimal choice. If the SEM is also equipped with energy dispersive spectrometer, chemical compositional analysis can be carried out by excitation of the outer orbit electron. Although energy dispersive spectroscopy (EDS) is not useful for compositional analysis smaller elements, it can still give a relative reading showing which areas have a higher concentration. Similar to EDS, Auger electron spectroscopy (AES) uses the Auger effect instead which makes it more suitable and more accurate in identifying smaller elements.

In the case of the cracked steel frames, understanding the microstructure of the base material, along with the weld zone, is a critical first step in developing a direction for experimental testing. The embrittlement types of interest (liquid metal, hydrogen, and temper) all rely on the metallurgy of the material to some degree. Furthermore, the metallography of the material would show if there were any irregularities in the structure leading to embrittlement susceptibility. It is impossible to discuss the cause of cracking without first understanding the structure and constituents of the material.

In addition to metallography, fractography also serves as a backbone of knowledge on which

further studies are based. Fractography is the study of a material's fracture surface. It is a routine practice in the world of failure analysis, and similarly to metallography, is heavily based on imaging and recognizing characteristics [12]. Different failure types exhibit different features on the fracture surface created by the crack [13]. This helps engineers target the cause of failure and the fracture mode that occurred.

Similar microscopy techniques from metallography are also used in fractography. Once again, optical microscopes are often used as the baseline tool. However, SEMs are still extensively used since more often than not, higher level magnification images of the fracture surface are needed [12]. SEM imaging used in conjunction withe EDS is particularly useful since it can help identify any constituents on the fracture surface that may lead to the cause of cracking.

Even something as simple as a visual inspection for plastic deformation is very beneficial to the case of the cracked steel platforms. Plastic deformation of the material would be an expected feature of the fracture of a structural steel. However, the absence of deformation and relatively flat fracture surfaces would indicate some sort of embrittlement phenomenon is at play, rather than a simple case of plastic collapse. Further details of the surface can be observed under the SEM such as grain deformation, and elemental analysis can be done by EDS. Altogether, the metallography and fractography studies were a cornerstone in the investigation of the cracked steel frames, and gave valuable knowledge into structural steel metallurgy and fracture modes.

2.2. Methods and Experimental Setup

Sections were cut from the base material of the provided samples. Base material samples were taken from three different joints (six different steel beams), along with cross sections of the welds. The joints were cut using a band saw to isolate the beam's flanges and the weld seams. Images of the cutting and the flanges are shown in Fig. 2.1. Next, using a wet abrasive saw the samples were cut to be mounted in a 1.25 inch mold.

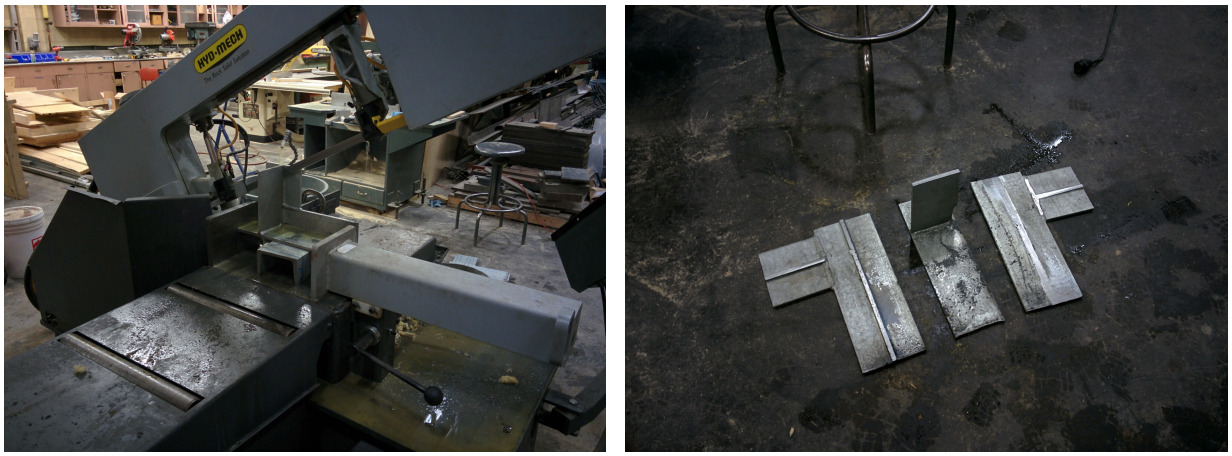

(a) Band saw cutting

(b) Removed sample flanges

Fig. 2.1: Sample cutting

To prepare the sample to be seen under the microscope, it must first be ground, polished, and then etched. Samples were ground using 240 grit SiC sandpaper until the surface was flat to a visual inspection. Following the 240 grit sandpaper, 360, 600, and 1200 grit SiC sandpapers were used at approximately two minutes per grit grade. In some cases this was done longer to eliminate any scratches and ensure a fine surface. Following grinding, 3µm, 1µm diamond suspensions and 0.5µm along with 0.05µm alumina suspensions were used progressively for polishing. The samples were etched using a 5% nital (5% nitric acid and 95% alcohol) for approximately 15 seconds. A few samples were also treated using a picral etch (4% picric acid and 96% alcohol).

A SEM and optical microscope were used for capturing images of the microstructure, along with the crack initiation site and arrest points. Operation of the optical microscope is relatively simple, as the mounted sample is placed on a stage and through a system of optical lenses and focused light, an image of the sample is projected. However, operation of the SEM is more complex. The samples are first taken out of the epoxy mount and placed on a stage using copper tape (for optimal electron conduction). The stage is then placed in a chamber that is vacuum sealed. The samples are then excited with a beam of electrons, which causes the sample to give off secondary electrons. By reading the secondary electrons from the sample an image of the topography is produced which is the high magnification image of interest. In addition, the EDS operates by reading the x-ray energy that is given off during the particle's excitation. The electron beam excites an electron on an inner shell of the particle causing it to eject. An

electron from a higher energy outer shell fills the electron hole left by the ejected electron, and the difference in energy is the x-ray given off. The difference in energy between two shells is indicative of the particle's atomic structure and can thus be used to determine the elements [14].

Auger electron spectroscopy functions using a similar concept of excitation through an electron beam and ejecting a core electron. However, the difference between AES and EDS is that instead of measuring the energy difference in the form of X-rays it is measured by the emittance of a second electron called the Auger electron. This process is called the Auger effect [15]. AES is a more suitable option for measuring smaller elements such as carbon and was used for carbon mapping and sulfur mapping. The surface of the samples analyzed by AES were prepared in the same way as the SEM samples. In addition, the surface cleaned with ion sputtering to expose a fresh surface for elemental mapping [16, 17].

Unlike the metallography samples, the fractography samples did not require the same amount of preparation since the fresh fracture surface is the area of interest. The cracks were cut open to expose the fracture surface. The surfaces were first inspected visually for any macroscopic features such as plastic deformation or beach marks. The fracture samples were then cut to an appropriate size to fit on to the SEM stage and were mounted using the same copper tape process. The fracture surface was observed at high magnification using the SEM and constituents were studied using EDS.

2.3. Results and Discussion

2.3.1. Metallography

Images showing the microstructure of the samples taken from a T-joint are given in Fig. 2.2. These images show the samples etched with a 5% nital mixture to give a well defined image of the grain structure, size, and any inclusions. The lighter grains are ferrite, since the nital etch would not corrode the ferrite quickly. The darker grains are a carbide formation, but there are also inclusions present. It is also interesting to note that in the 50X magnification images, some grain boundaries appear thicker than usual or than expected. This implies the presence of carbides and inclusions in the grain boundaries.

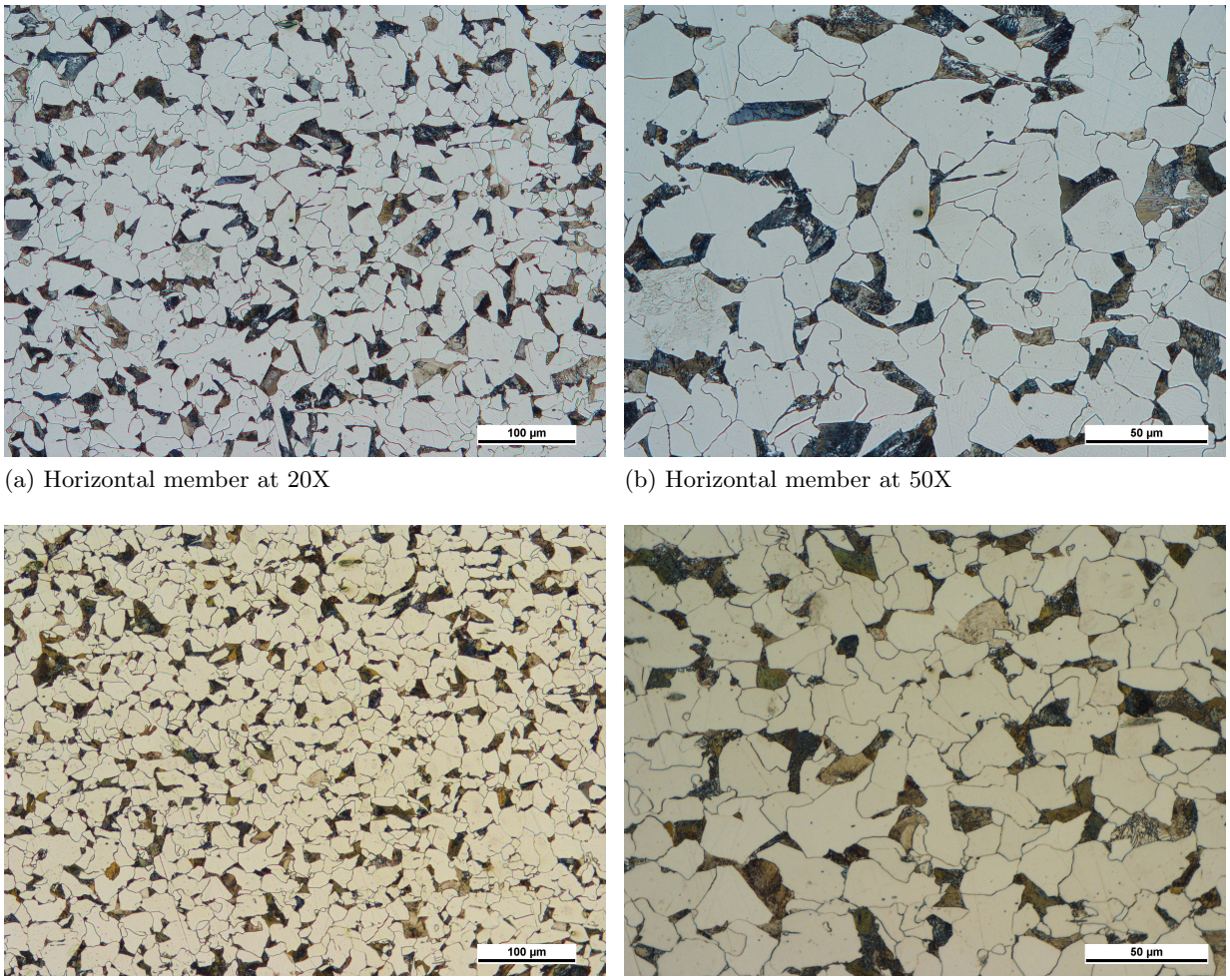

(a) Horizontal member at 20X

(b) Horizontal member at 50X

(c) Vertical member at 20X

(d) Vertical member at 50X

Fig. 2.2: Base material of the T-joint

The corner joint samples show similar features and the same carbide formation. Images showing the base material at different magnifications are displayed in Fig. 2.3. Similar thick grain boundaries or small carbide formations are seen in image Fig. 2.3(c). Further optical microscope images of the base material's microstructure and varying magnifications can be found in Appendix A.

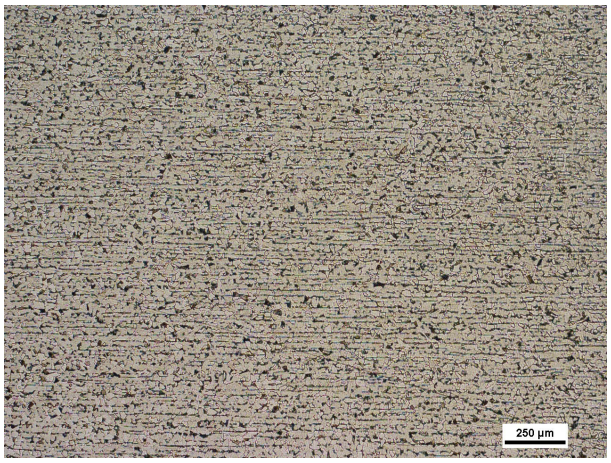

(a) Corner joint base material at 5X

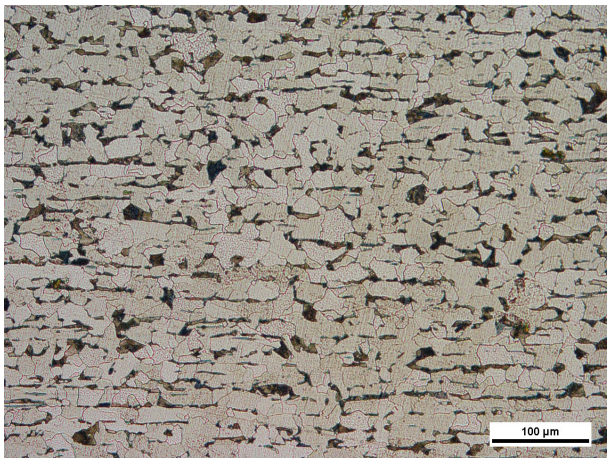

(b) Corner joint base material at 20X

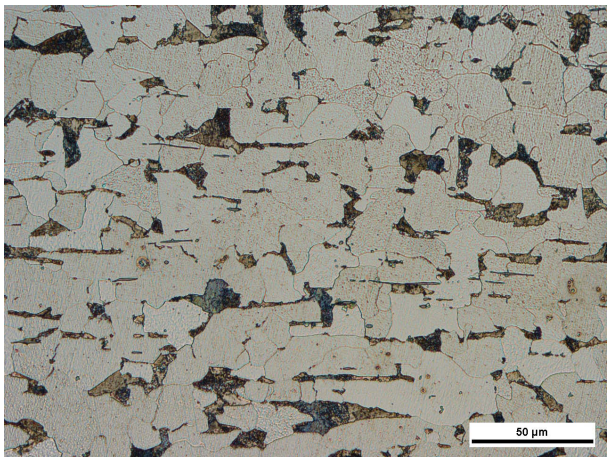

(c) Corner joint base material at 50X

Fig. 2.3: Base material of the corner joint

To definitively determine the carbide structure that makes up the darker grains, the picral etch was used was used on the corner joint base material. Images showing the same location with the nital etch and picral etch for comparison are shown in Fig. 2.4.

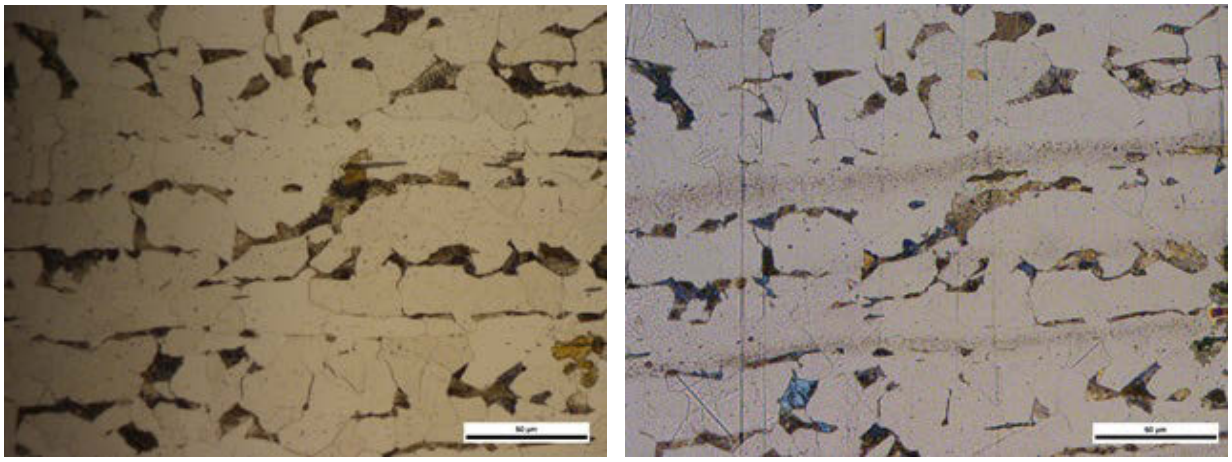

(a) C-channel base material using nital etch (b) C-channel base material using picral etch

Fig. 2.4: Images showing the same location with the different etchants

As expected, the picral etch shows pearlitic grains as the structure of carbide formation. This is evident by the somewhat lighter colour carbides meaning ferrite is present, and in the grains that were exceptionally well captured a layered structure can be seen [18]. The final and most definitive step to confirm the pearlite grain is to analyze the samples with the SEM for highly detailed topographic image. Two images showing the grain structure from the SEM can be seen in Fig. 2.5. Fig. 2.6 also shows a carbon map produced by AES. It should be noted there is a high carbon concentration in the grain boundaries as well as the pearlite grain.

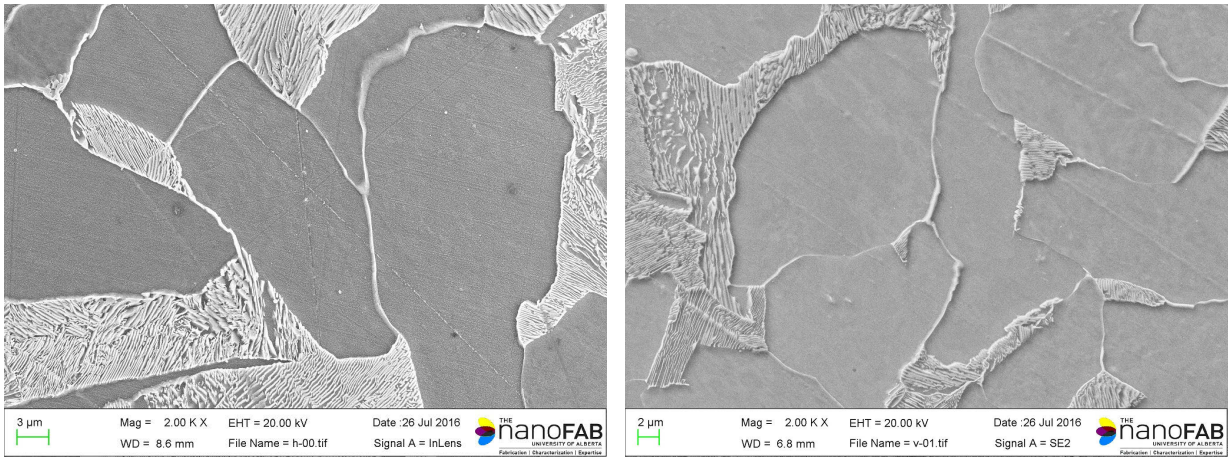

(a) Horizontal member 2000X (b) Vertical member 2000X

Fig. 2.5: SEM images of the T joint base material

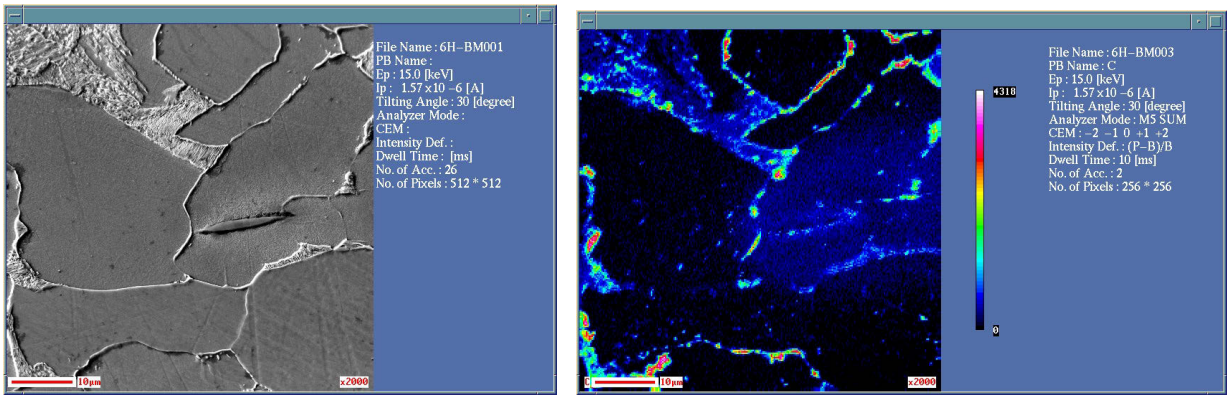

(a) AES Location (b) AES Carbon Map

Fig. 2.6: AES carbon mapping

The thicker grain boundaries are an interesting observation and could be a critical clue in the investigation of the cracked platforms. Once again in Fig. 2.5, thicker grain boundaries are seen. Grain boundary segregation is an important factor for temper embrittlement; however, key elements must be present. To analyze the make up of the thicker grain boundaries, EDS line scans were used. EDS line scans do not give an exact composition of the grain boundary (which may be considered inaccurate for smaller elements anyway), but it will give a relative reading, in case the concentration of certain elements is higher at the grain boundary. This will give an idea of what elements the grain boundaries are composed of. Two different sites and their EDS scans are shown in Fig. 2.7 and Fig. 2.8.

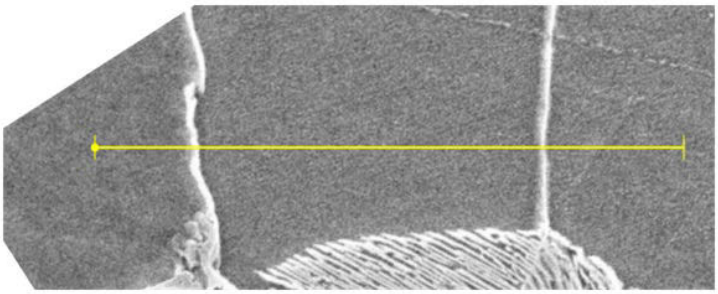

(a) EDS line scan site A

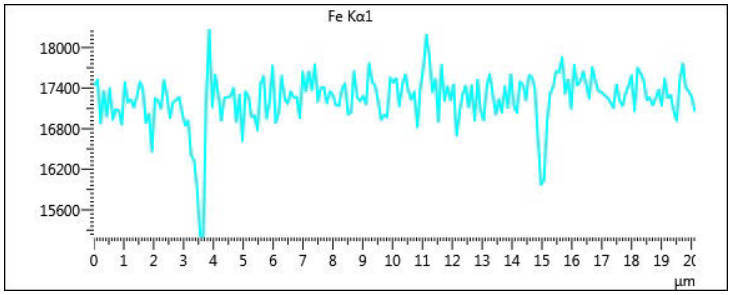

(b) Fe EDS line scan site A

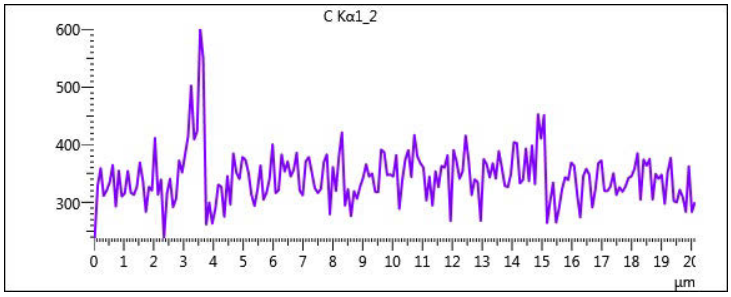

(c) C EDS line scan site A

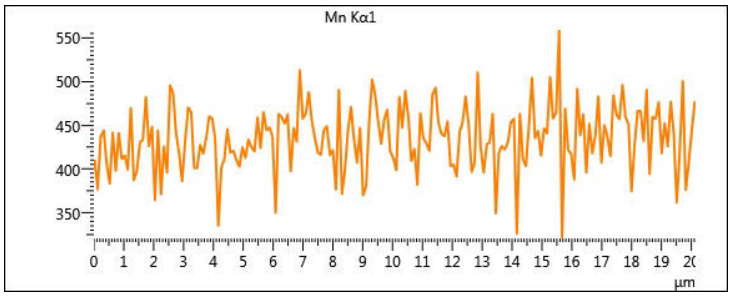

(d) Mn EDS line scan site A

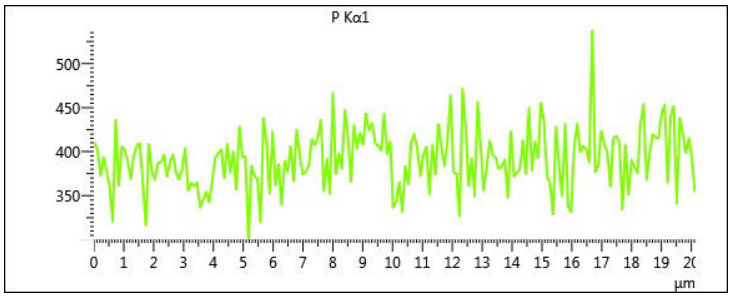

(e) P EDS line scan site A

Fig. 2.7: EDS line scans of site A

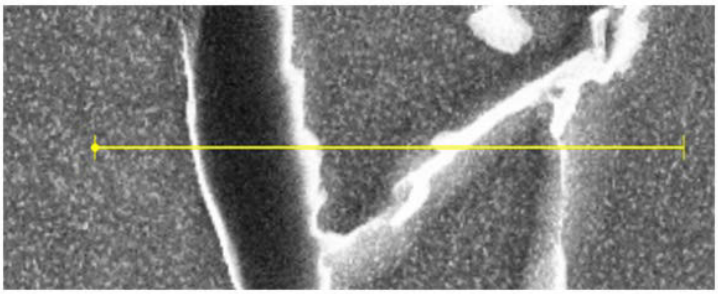

(a) EDS line scan site B

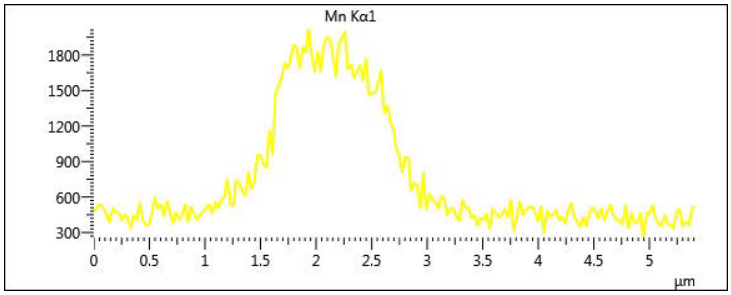

(b) Mn EDS line scan site B

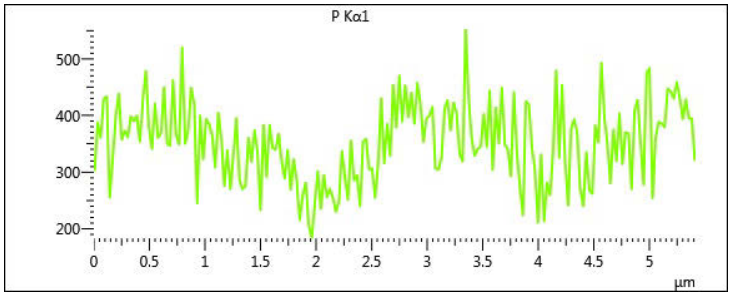

(c) P EDS line scan site B

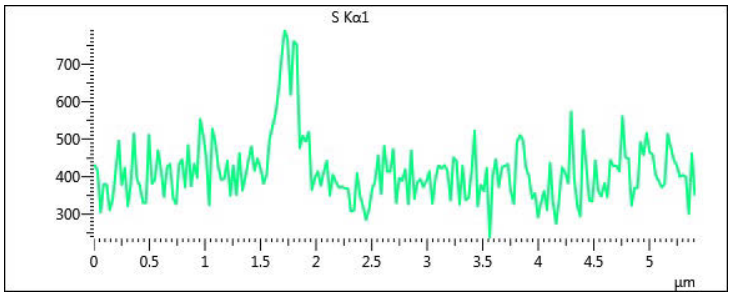

(d) S EDS line scan site B

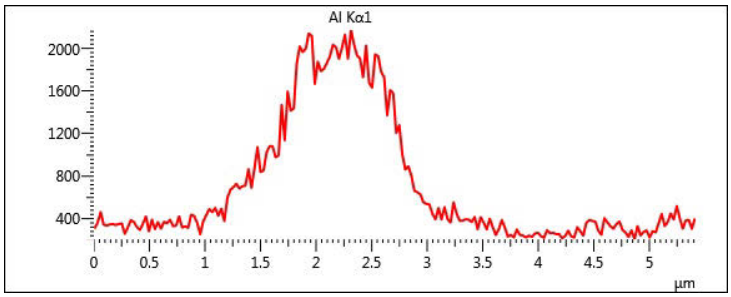

(e) Al EDS line scan site B

Fig. 2.8: EDS line scans of site B

When looking at the results of site A in Fig. 2.7, there is a clear dip in the iron content at both grain boundaries. This is expected as the ferrite grains would have much higher iron content than the grain boundaries, but also shows it is not cementite that has formed. Carbon however has a large spike on the first grain boundary and a relatively smaller spike on the second. In contrast, both manganese and phosphorus only spike on the second grain boundary. These results would indicate that some type of carbide has formed on the first grain boundary and the second grain boundary is made up of segregated impurities. The rise of phosphorus content in the second grain boundary is a significant finding, however, since it is directly related to temper embrittlement. Manganese is also reported to be a culprit element in temper embrittlement susceptibility; however, it is well documented that phosphorus is the main element of concern when dealing with temper embrittlement [10, 19–24]. To study this further, a separate site on a separate sample was used. Site B shows not only a line scan across a grain boundary, but also across an inclusion. It can be seen from the results that going across the inclusion spikes aluminum, manganese, and sulfur towards the edge. However, the grain boundary once again appears to spike the phosphorus content. The manganese content may also be higher in the grain boundary, but due to the large amount of manganese in the inclusion, the spike may not be detectable from the scan. Overall, the phosphorus content spiking at the grain boundary is a key finding and is cause for further investigation and testing into temper embrittlement.

To follow up with the line scans of the inclusion in site B, an area of the base material was found with several inclusions present. An EDS element map was created for the area to identify which elements the inclusions are composed of. The images of the EDS mapping as well as the inclusions are shown in Fig. 2.9

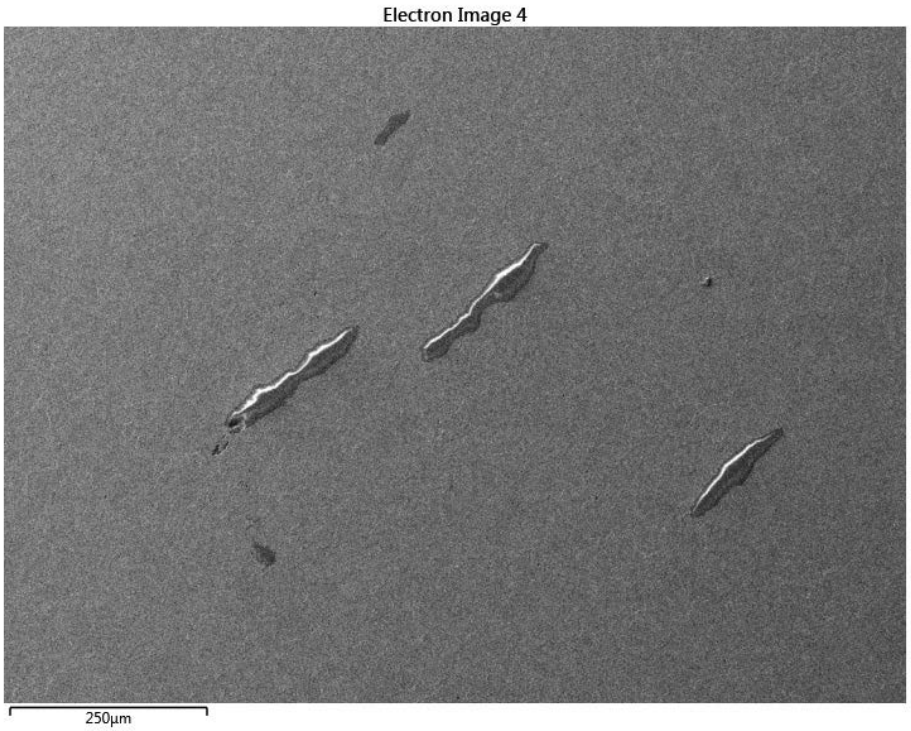

(a) Inclusion and mapping site

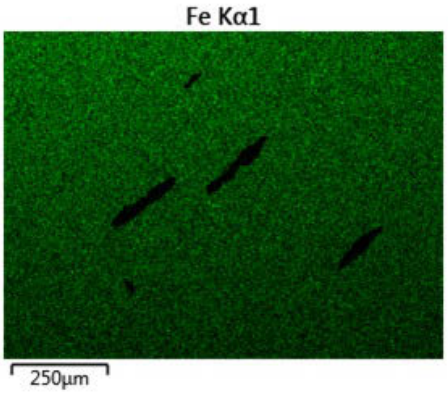

(b) Fe EDS map

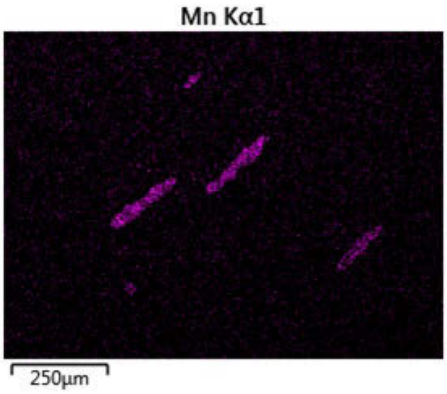

(c) Mn EDS map

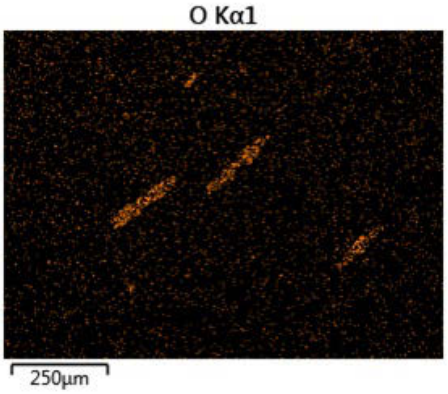

(d) O EDS map

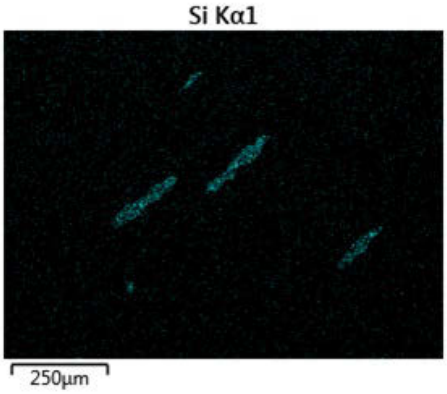

(e) Si EDS map

Fig. 2.9: EDS mapping of inclusions

The inclusions are mainly composed of manganese, silicon and oxygen. This is typical of 350W steel and is not a cause for concern. Other inclusions may be found within the steel composed of manganese and sulfur (as perhaps in Fig. 2.8) which is also typical of structural steel since the manganese will bond and consume the excess sulfur.

2.3.2. Fractography

When turning our attention towards the crack themselves, it is logical to first analyze the initiation site. Unfortunately, due to the crack opening in the galvanizing bath, the surface of the primary (macroscopically visual) crack's initiation is covered with zinc. However, Fig. 2.10 shows the crack initiation site and more specifically a secondary crack that microscopically formed alongside the primary crack, with a separation along the grain boundaries. This secondary crack is useful for analysis since the primary crack's initiation site cannot be seen. When zooming in on the secondary crack, as seen in Fig. 2.10(b), there is no deformation of the grains and the crack appears as if it could fit back together. It appears the crack is a result of separation along the grain boundary with no considerable plastic deformation. Each of these samples was sectioned and processed the same as the base material samples using a 5% nital etch. More images of the crack initiation site can be found in Appendix A. They are accompanied by images of the weld cross section, side view, and microstructure.

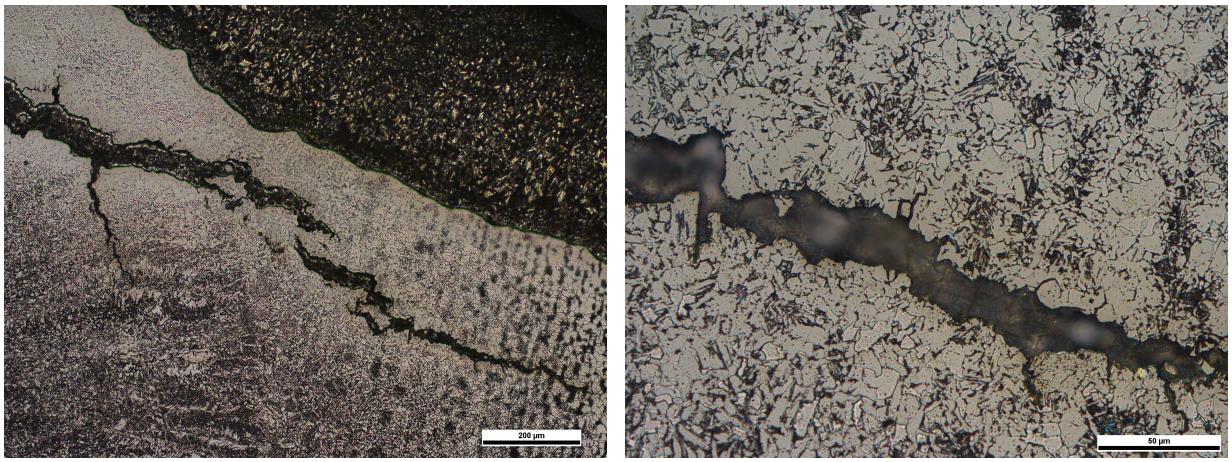

(a) Crack initiation site 10X

(b) Crack initiation site 50X

Fig. 2.10: Crack initiation site

Along with the crack initiation site, the arrest site is also of interest. An image showing the crack arrest is shown in Fig. 2.11. It can be seen that the crack has the same feature of grain

boundary separation with little to no distortion. This would imply the mode of fracture stayed the same throughout the crack propagation. An EDS map was done directly at the crack arrest, where from the microscope image it looks as though there may be something in the crack. The EDS map results are shown in Fig 2.12.

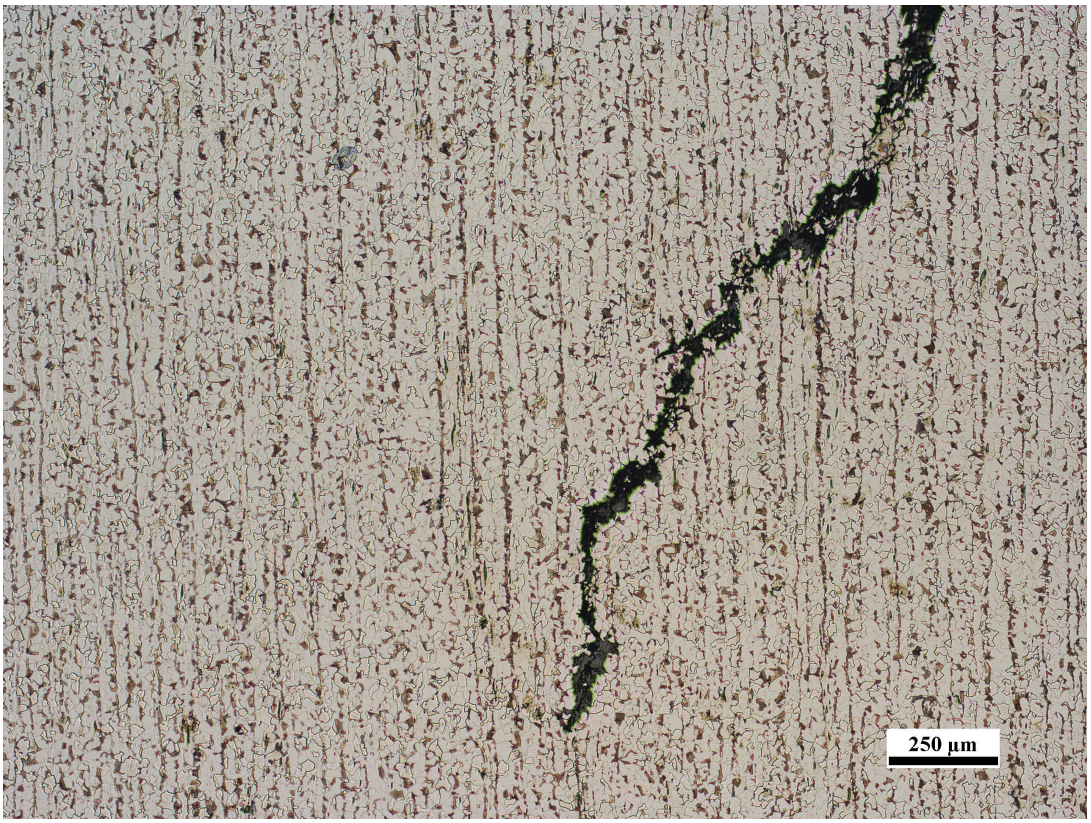

Fig. 2.11: Crack arrest site 5X

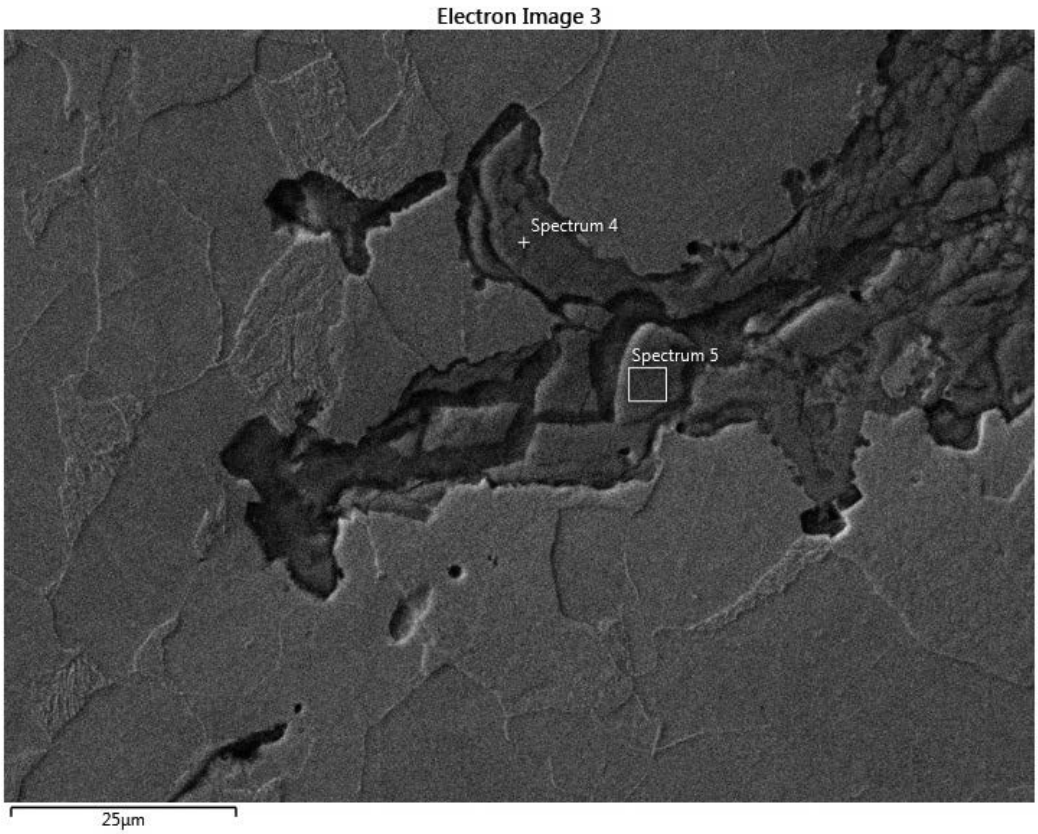

(a) Crack arrest site

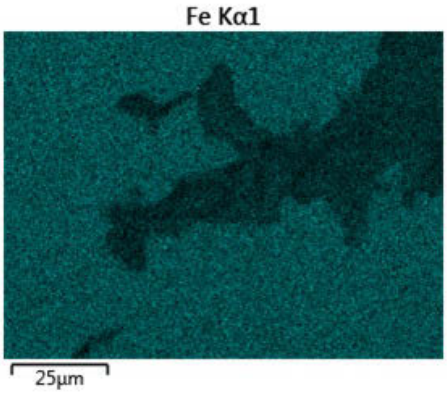

(b) Fe EDS map

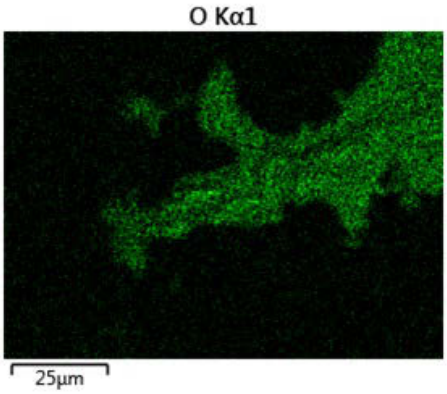

(c) O EDS map

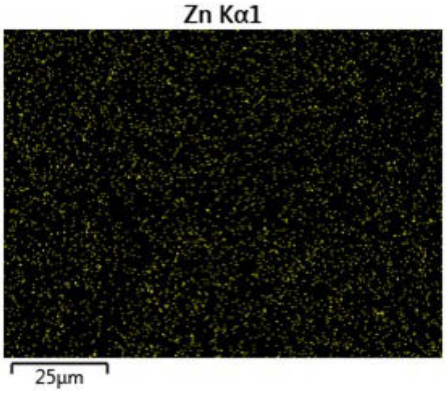

(d) Zn EDS map

Fig. 2.12: EDS mapping of the crack arrest

The results shown in Fig. 2.12 do not show anything irregular or noteworthy. There is no increase of zinc content in the crack, which suggests LME may not be the embrittlement case [8, 25]. Also, there seems to be a build up of oxidation in the crack, which is the inclusion that was seen from the optical microscope images. This may be due to the water used while grinding the sample or from exposure to the air, but in either case it is not unexpected.

The original cracked samples provided by the industry partner were cut and sectioned to expose the fracture surface. The surfaces show no signs of significant plastic deformation. They also showed brittle chevron markings, and some were covered with zinc while others were not. Images of three different fracture surfaces along with the overall sample can be found in Fig. 2.13.

(a) Cracked Sample

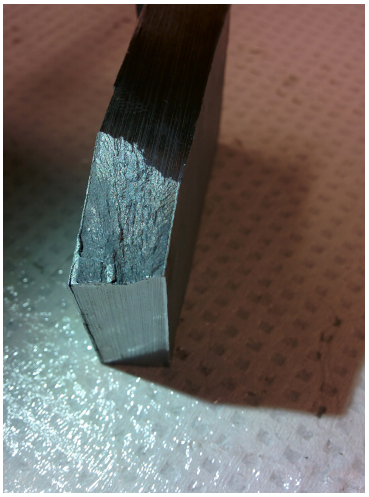

(b) Fracture A

(c) Fracture B

(d) Fracture C

Fig. 2.13: As received fracture samples

SEM images were also taken of the fracture surfaces. Images showing a 200X and 500X magnification of the fracture surface are given in Fig. 2.14. Fig. 2.14(b) shows dimple features on the surface in sizes of 20µm and up.

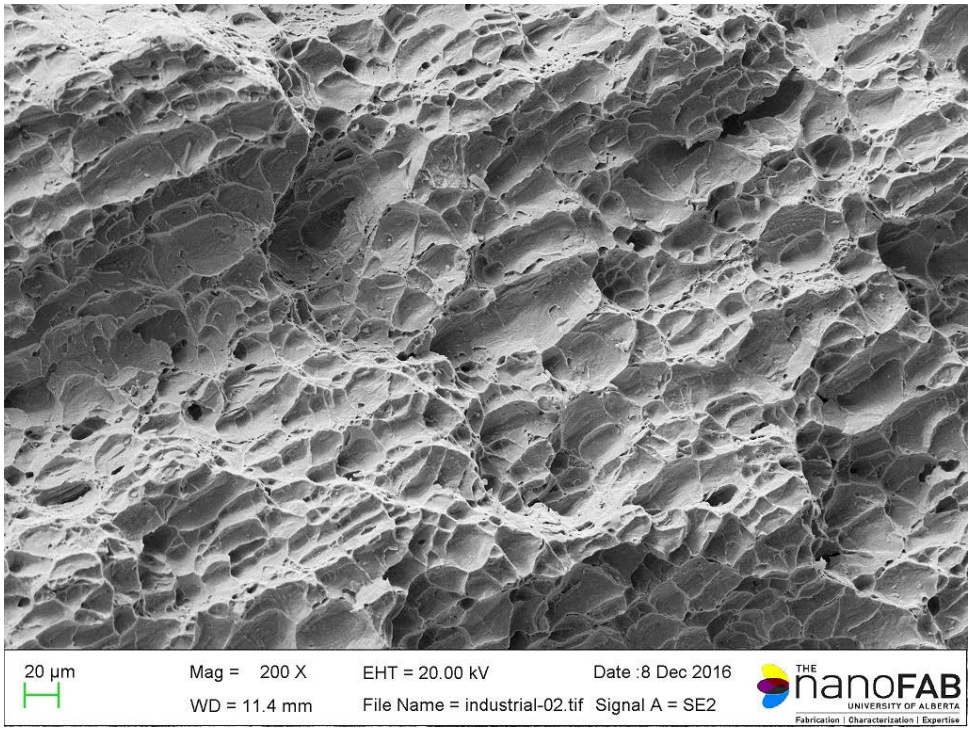

(a) Fracture Surface at 200X

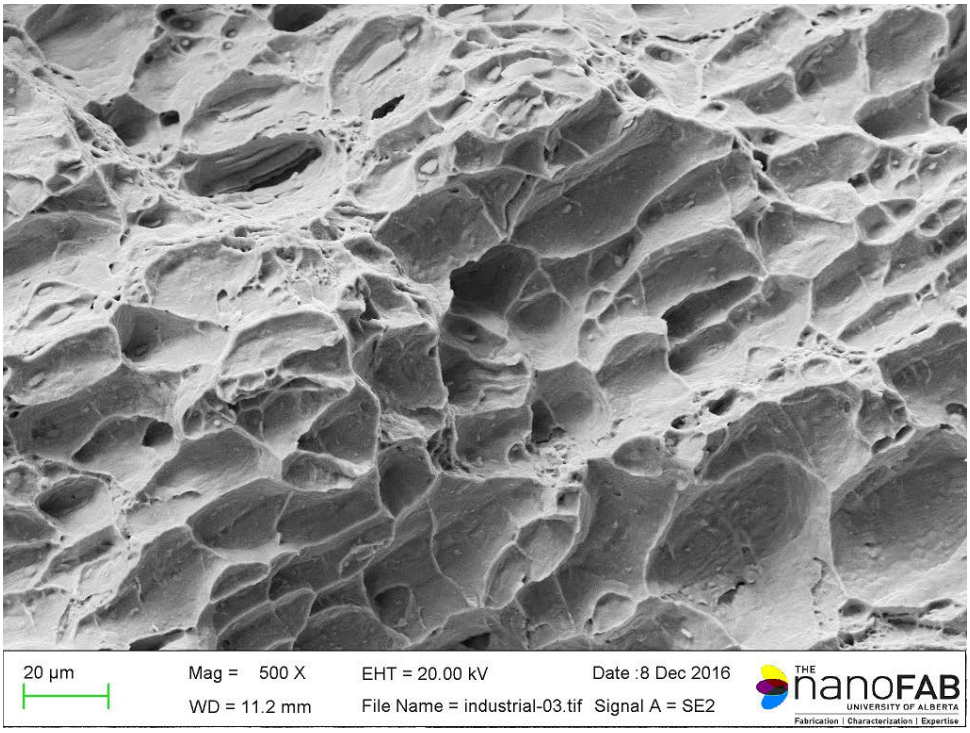

(b) Fracture Surface at 500X

Fig. 2.14: SEM of received fracture surfaces

In comparison, a fresh crack was made by fracturing the same base material at ambient temperature. An SEM image of 500X magnification is shown in Fig. 2.15. In comparison to the features seen in Fig. 2.14(b), the dimple features are much smaller. The largest dimples are about 10µm with many smaller dimples across the surface.

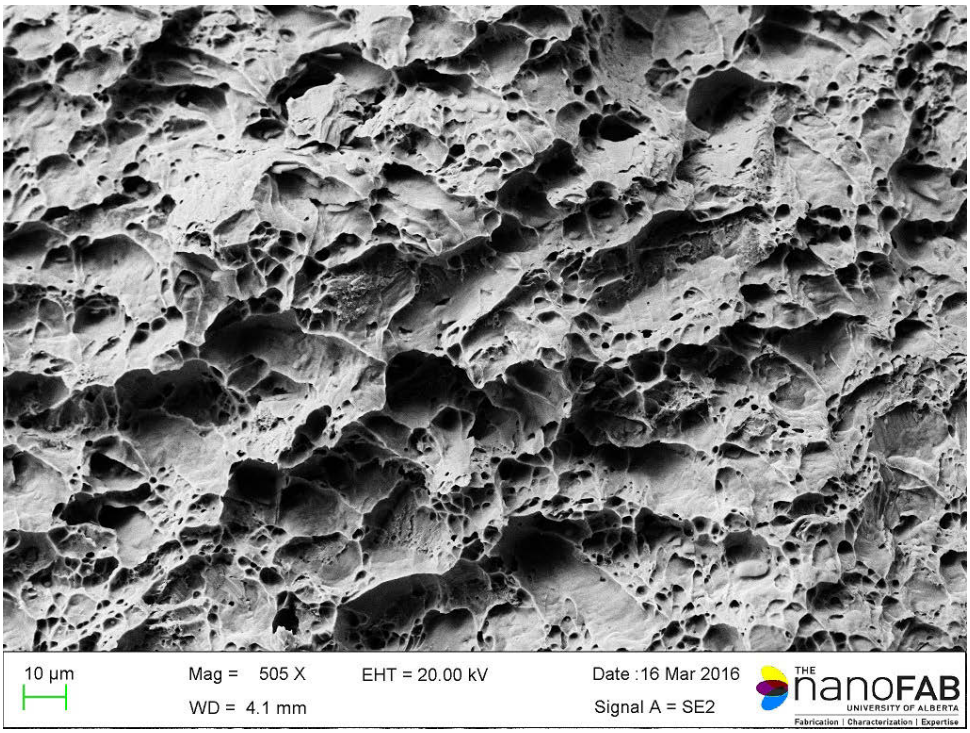

Fig. 2.15: Fresh fracture surface

Looking at the images of the provided samples, it can be seen there is little to no deformation of the steel on the fracture surface. It does not show any characteristics of ductile fracture, such as cup and cone features or plastic deformation. Furthermore, when examining the fracture surface under the SEM there is no evidence of deformation of the grains, the dimples seen are the same size as the grains (20µm), and the surface shows smooth areas between the grain boundaries. Even more explicitly in Fig. 2.15, microvoids can be seen across the surface. Given the distinction in these features, the difference in fracture mode can be seen directly when comparing Fig. 2.13 and Fig. 2.15. Given that 350W is expected to have very ductile behavior, the brittle fracture mode in the provided samples is critical to determining why the steel platforms cracked and supports the notion of an embrittlement factor present.

With the findings of this chapter, it is clear experimental testing is needed to further explore the embrittlement factor at play. There is evidence to suggest temper embrittlement may be

the case but testing is also needed on hydrogen embrittlement. Also, a FEA model is needed to place metrics on the stresses of the double dip galvanizing process. The conclusions of this chapter have given a base of knowledge and clues into the cracking of the steel platforms which can now be followed up with experimental lab testing.

2.4. Conclusions

The microstructure of the steel base material was analyzed using an optical microscope and SEM. The images show a typical ferritic and pearlitic steel microstructure which is expected of 350W and 300W steel. However, a closer inspection shows thicker grain boundaries with potential grain boundary segregation. EDS analysis shows the thicker grain boundaries are composed of either carbides, manganese, or phosphorus. EDS analysis also showed the inclusions were not composed of anything detrimental.

When analyzing the cracks that occurred during galvanizing the most outstanding result is the absence of any ductile features. There are no visual signs of plastic deformation, which is very uncharacteristic of the steel. It can be said the fracture during galvanizing was brittle. However, when the steel is fractured at the ambient temperature, it is ductile. Therefore, an embrittlement factor must have been present during the cracking of the steel platforms. In addition, the cracks showed little to no zinc on the crack surface. Zinc is only found consistently at the opening of the crack. This suggests LME was not the cause.

3. Finite Element Analysis Model

3.1. Introduction

Finite element analysis is a numerical method for solving complex mathematical problems in engineering as well as physics. In engineering it is typically used for problems involving structural analysis, fluid mechanics, or heat transfer. The basic concept revolves around dividing the existing problem into a discrete simpler problems called finite elements. The finite elements are solved individually by developing an equation for each element. Then once each element has an associated equation, they are put together as a global system of equations that models the original larger problem [26, 27]. The equations are simple local approximations of the original complex equation, which is usually in the form of a partial differential equation. In FEA this simplification is done using Galerkin's method [26]. To solve the system of equations, FEA relies on the boundary conditions. These must be known and accurately modeled for FEA to be useful. FEA can be used for static cases as well as transient cases.

The subdivision is often referred to as meshing. In the case of structural analysis, the mesh is the subdivision of the structure's geometry into smaller and standard geometric elements. The types of elements typically used in FEA meshing are tetrahydra, pyramids, prisms or hexahedra, for continuum models. Each meshing type has its own number of nodes, which is a point used for calculation during the FEA calculations [28]. Nodes are placed at the corners of the elements, on the elements faces, or in some cases, within the element. Elements are connected by the corner nodes, and when the nodes displace that will distort the connected elements in accordance to the inputted properties [29]. The nodal displacement is the basis from which outputs such as stress are drawn.

In some cases the nodes are the points being used for calculation, and the nodes cannot cover the entire model, the output may have a dependency on the mesh size. However, the critical mesh size for acceptable accuracy can be easily assessed. It is done by a mesh refinement study, which includes taking an important metric and studying the change of the result as the mesh refines. Once the result shows little change with large changes in the mesh refinement, the result is deemed independent of the mesh and of acceptable accuracy [30].

Use of FEA to model the hot dip galvanizing process it seems it is sparsely reported in literature.

Modeling the hot dip galvanizing process would include the self weight of hoisting the object, but it is primarily a heat transfer problem. Therefore the thermal stresses and their distribution would depend on the geometry of the hoisted item. For this reason, literature available does not focus on what kinds of stresses are expected during galvanizing. Instead studies have been found analyzing the beam distortion during galvanizing, and investigating the heat transfer that takes place. Although this study, along with others, does not give an idea of the stresses of galvanizing, the heat transfer properties are very useful for creating an FEA model of the cracked steel platform structures.

Abaqus FEA is one of the largest and most widely available software packages to conduct an FEA study. Although FEA is a numerical method, the user interaction with *Abaqus* is largely visual. A two or three dimensional model is created and the boundary conditions are visually applied by selecting the node, line, or surface for their location. Loading is done in a similar fashion, whether it is mechanical or thermal. The intricacies and complete details of the *Abaqus* software functions are beyond the scope of this chapter, however the visual operation and results of the software are greatly valued in the case of the cracked steel platforms. The shape of the stress distribution across the structure is just as significant as the stress values themselves.

Using FEA to analyze the cracked platforms gives many insightful results in terms of what the platforms experienced during the double dip galvanizing process. Using the *Abaqus FEA* software, a solid model of the platform can be created and analyzed for the stress experienced during the dipping procedure.

3.2. Model Methodology and Setup

Along with the physical joint samples, plenty of documentation and drawings were provided of the steel platform structures by the industry partner. These drawings were important initially to determine where the samples had been sectioned from. However, the drawings include dimensions as well as the assembly list which includes the individual beam dimensions and profile type. There is also many section views available to fully understand the connections and fit between beams. An image of the drawing is shown in Fig. 3.1.

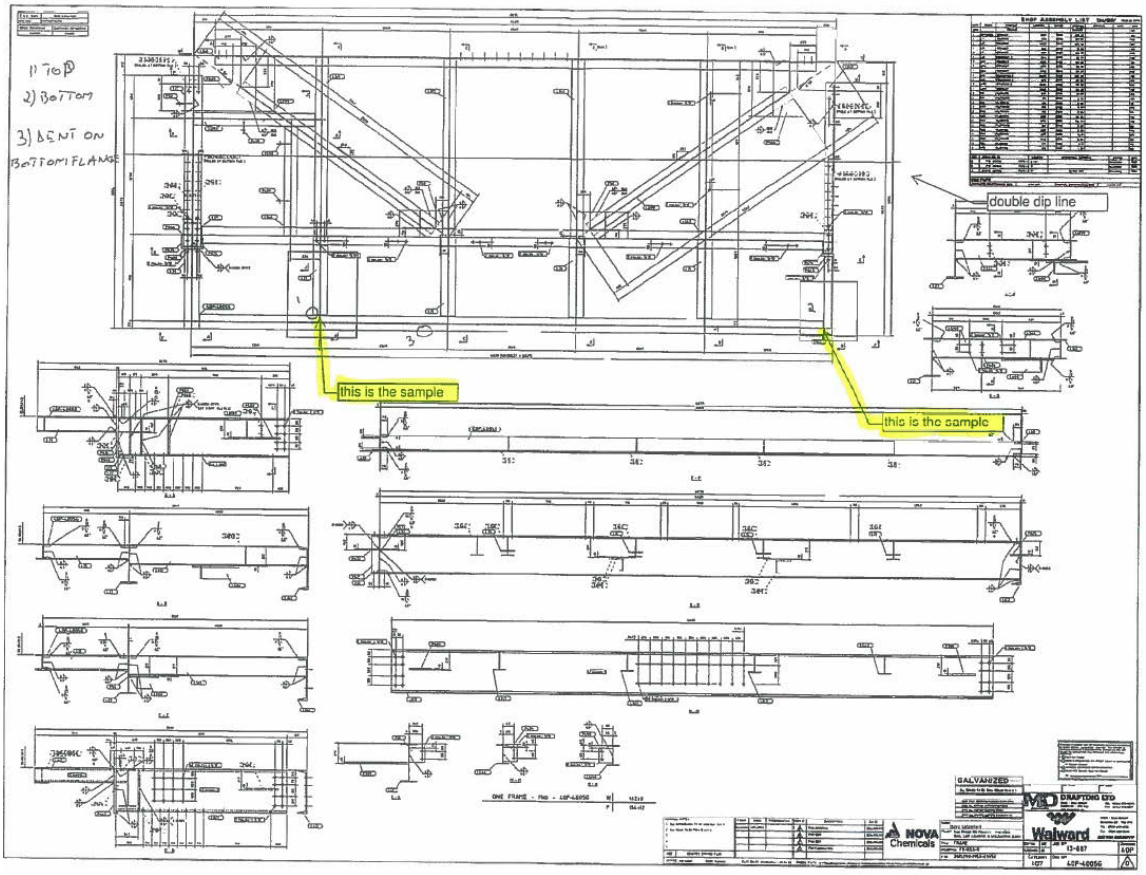

Fig. 3.1: Platform assembly drawing

This first step to creating an FEA model in *Abaqus* is to create a three dimensional solid model. The drawing seen in Fig. 3.1 was the schematic used for creating the solid model, and the model was made to match the drawing exactly. Each beam profile was first sketched, and then each beam in the assembly was extruded in accordance to the listed length, and the material properties of the structural steel were applied to each section. Once all the parts were created, the connections could be modeled. The drawing shows that all the joints are done via welding, however given the complexity of modeling a weld in FEA it is a common assumption to assume it as an ideal connection. Once the FEA is carried out, this will show the stresses at each joint without any independent movement of the members. This will keep the deformation of the frame as a cohesive unit, which is how it is assumed a perfectly welded structure would be behave. This connection is modeled using a tie constraint in the software. The tie constraint requires selecting a master surface and slave surface, where the nodes of the slave surface are adjusted to match the master surface. This allows for the seamless connection between the two parts. Fig. 3.2 shows the assembled three dimensional model along with a close up of a T-joint

and the tie constraint.

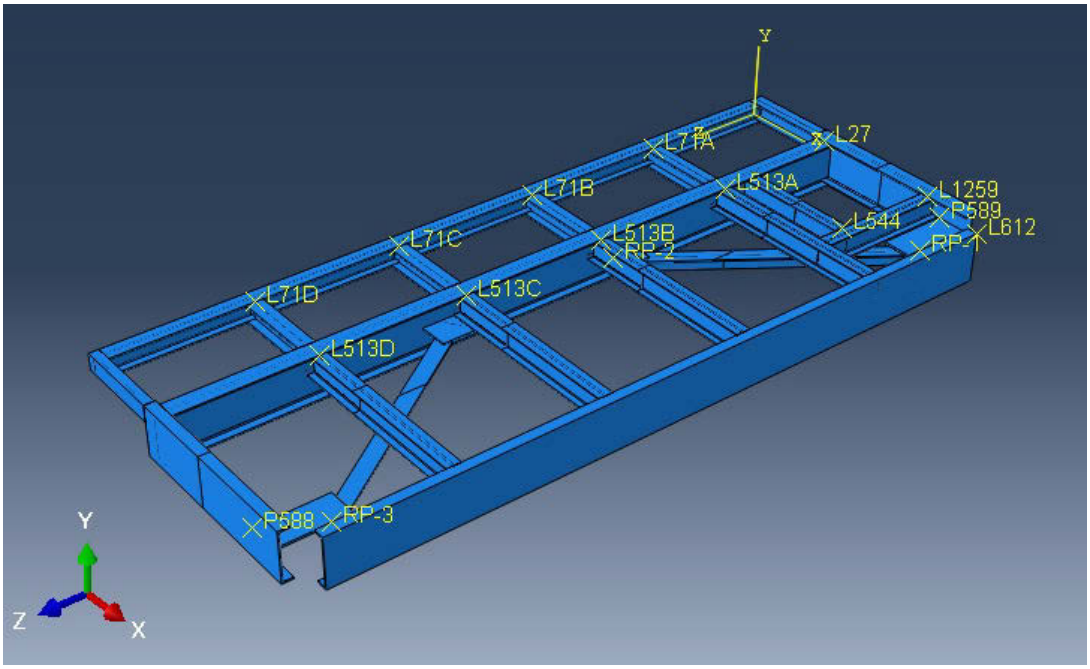

(a) 3D model

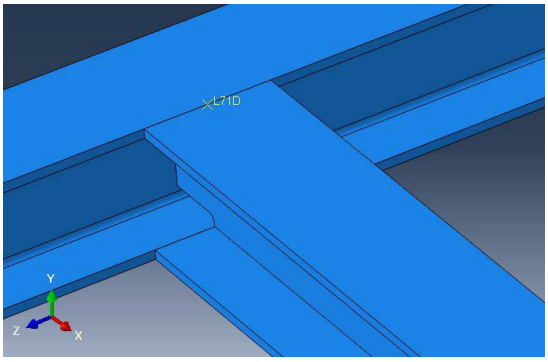

(b) T-joint connection

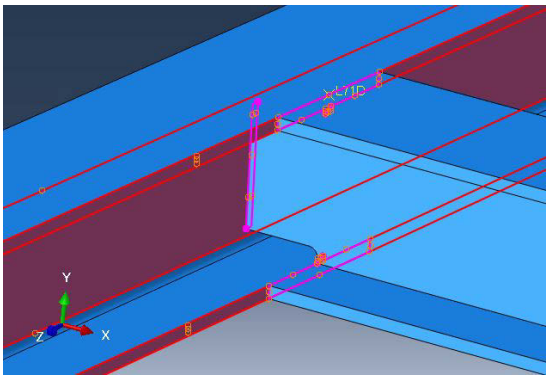

(c) Tie constraint

Fig. 3.2: 3D model of the platform and joint constraint

Once the three dimensional model has been created, the frame work of the FEA model can be set. First, to create a time dependent model the steps must be created as transient. Steps are generally used to separate different phases within the model. For example, in the double dip of the steel platforms, four steps were used: the hoisting of the platform, the first dip, the cool off between dips, and the second dip. As a transient step, the time period must be inputted from which the software creates incrementation to show the frames that best capture the changing states. The increments have a minimum value (such as 0.0001) and the maximum value is equal to the time period (in the case that nothing changes throughout the time period). For the

double dip process a time period of five minutes was used for the submersion time and the cool off was extended until the frame returned to the ambient temperature. This is assumed given that the workers would need to be able to work around the structure and handle it before doing the second dip.

After putting the steps in place, the boundary conditions and loads can be created and applied to the structure. The first step only included the hoisting of the frame, and was created to be able to see the stresses of hoisting alone. In this step the loading is purely mechanical and is a result of the self-weight of the platform. According to the commercial galvanizing company, the structure was hoisted using two chains around the corners of the structure. To model this as a boundary condition the line of nodes at the corners was fixed to have zero displacement. Fig. 3.3 shows the application of the boundary condition to the platform's corner. The software has a loading function available that is self-weight of the structure (assuming the density of the parts is inputted) where the only input needed is the acceleration due to to gravity which was set at $9.81 m/s^2$.

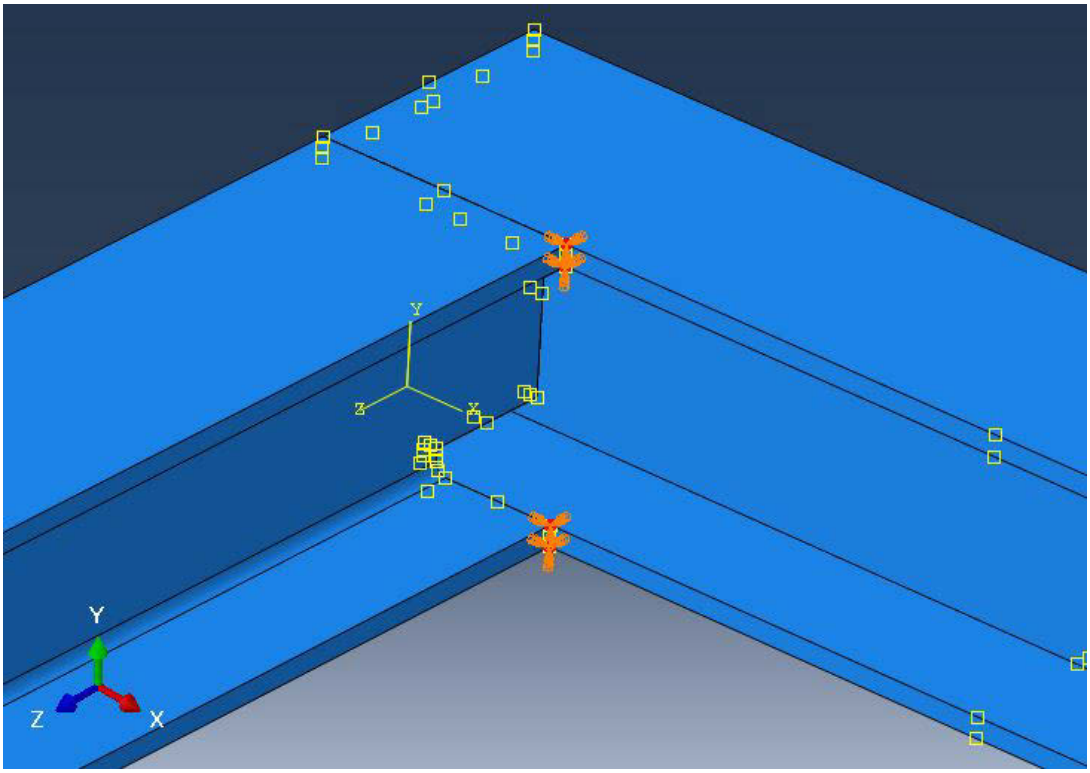

Fig. 3.3: Location of boundary condition

The remaining steps focus heavily on modeling the heat transfer of the dipping process. The

parameters that are known about the heating during galvanizing are only the dwell time in the molten zinc bath and the temperature of the bath at 450 °C. Thermal loading in *Abaqus* is done by different forms of heat fluxes, however given the information that is available, modeling the heat transfer directly as a flux would be very difficult. Instead, the software has another option to create an interaction between the structure and the inputted environment. Using an interaction, a convection heat transfer can be modeled. With the convection coefficient of $1350\,\mathrm{Wm^{-2}K^{-1}}$ from the study of beam distortion during galvanizing, all the required inputs are known for the model [31]. A partition line is used to separate the model into two halves along the double dip line shown in the drawing. During the second step, the convection of the galvanizing bath is applied to half of the structure, while the convection of the ambient air is applied to the other half. A visual of the application area is given in Fig. 3.4. During the third step, the convection of the ambient air applied to the whole structure and finally in the last step the inverse of the first dip interactions were applied. It should also be mentioned that during the second dip the boundary conditions of the hoist are moved to the other ends of the structure and the force of gravity is reversed since it is being hoisted on its opposite side. The different interactions, loading and boundary conditions are activated and deactivated as the model progresses through the steps.

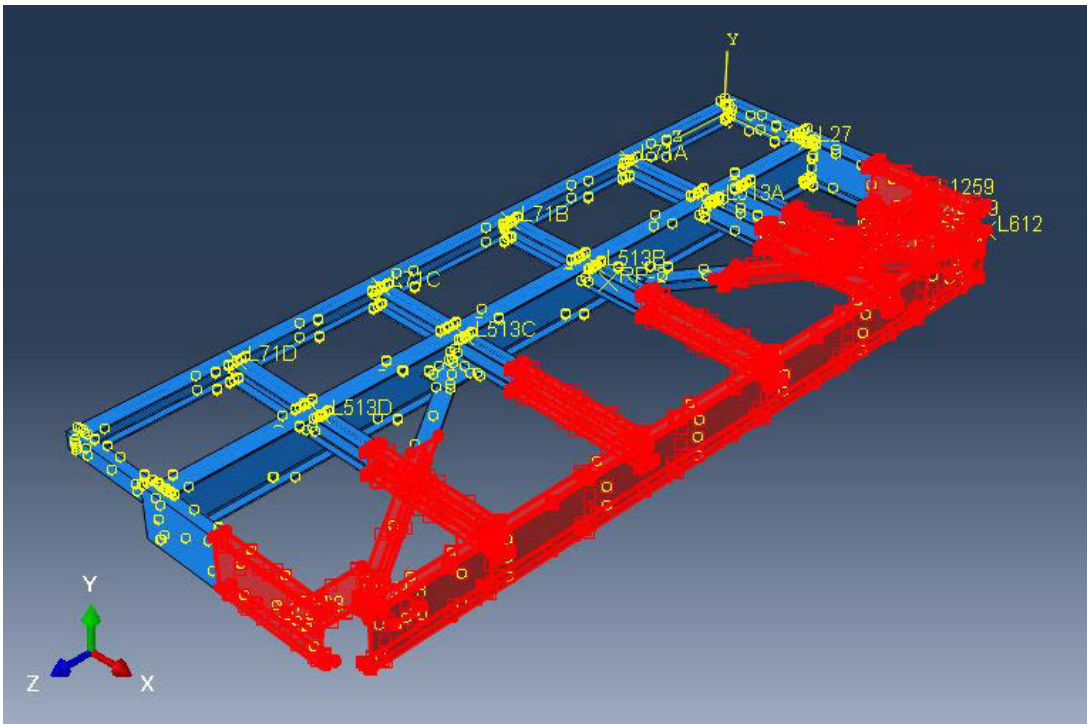

Fig. 3.4: Galvanizing bath convection area

Finally, a mesh must be created and refined for accurate results. Initially a coarse mesh is created for easy and quick computation. Tetrahedral elements were used since they are required for a thermo-displacement coupled computation. From there a node of significant interest is chosen and the results of that node are tracked as the mesh refines. For the steel platform model, a node in the area of cracking at the T-joint was chosen. Given this is a transient case, the peak stress during the whole galvanizing process was taken as the tracked metric. Once the peak stress was approximately stable and independent of the number of elements, the results were deemed reliable and accurate. This occurred with approximately 204 000 elements in the model.

3.3. Results and Discussion

The results of the mesh refinement study must be shown first, before analyzing the stress and temperature results. For this study, a node on the T-joint was chosen. Fig. 3.5 shows the T-joint with the node highlighted. It is important to note that the node at the exact edge where the cracking initiated can not be used for the study. Due to the method of computation of the software, edge nodes do not converge.

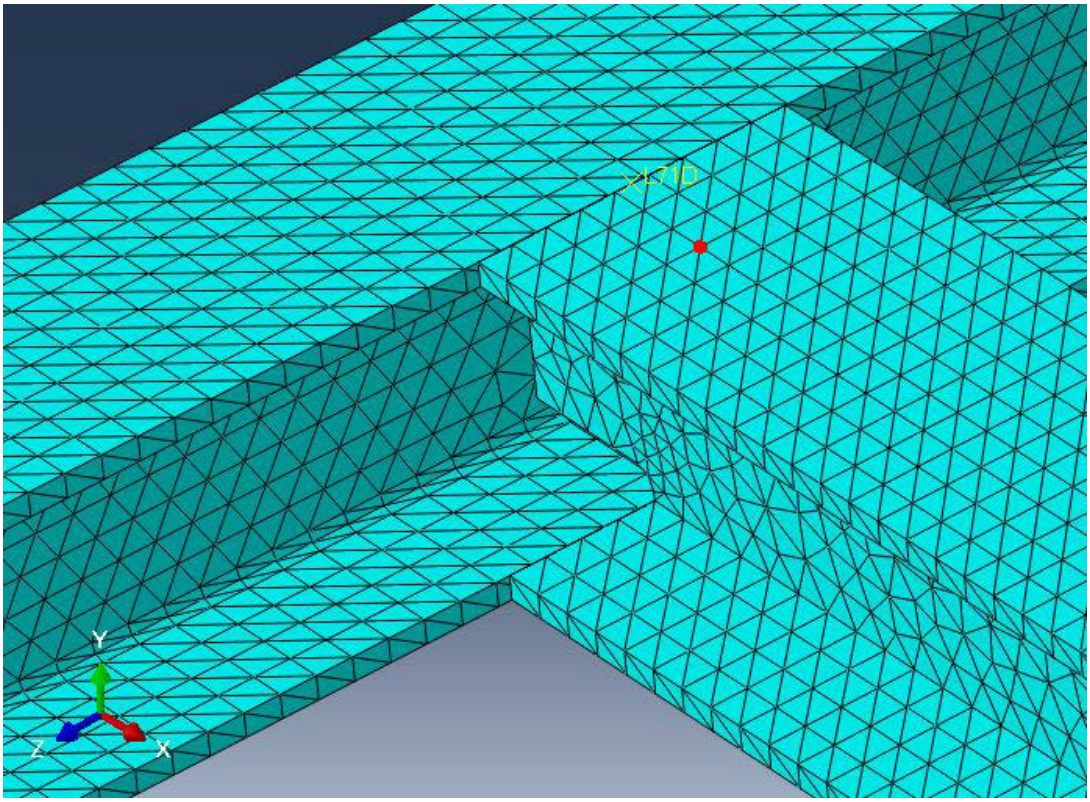

Fig. 3.5: Node chosen for mesh refinement study

As previously described, the coarsest mesh was initially used and refined until the results at the node in Fig. 3.5 showed very little change with a large change in the number of elements. The results of the study are shown in Fig. 3.6.

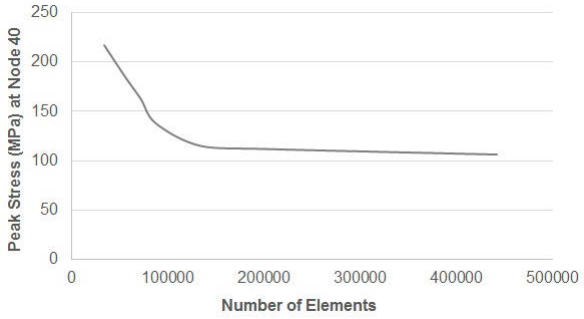

Fig. 3.6: Plot of nodal stress versus number of elements

The plot shows the stress value stabilize around 200 000 elements. The change from 200 000 elements to 400 000 is minimal considering the number of elements has doubled. A final number of approximately 204 000 elements was used for the FEA model. Fig. 3.7 shows an image of the final mesh applied to the model.

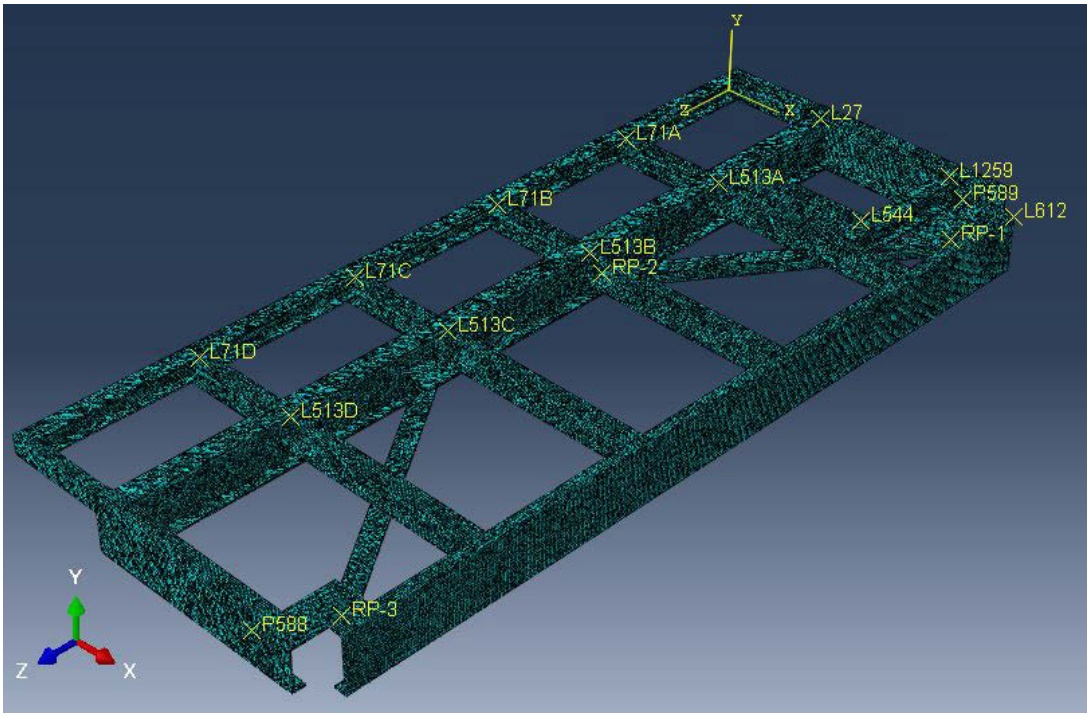

Fig. 3.7: Mesh applied to the model

Since the FEA model goes through multiple transient steps, the best way to capture the results is to select a node and track the stress experienced at that point. Two nodes were selected,

one at a corner joint and one at a T joint, for plotting the stress during the entire galvanizing process. A visual of the selected nodes is given in Fig. 3.8.

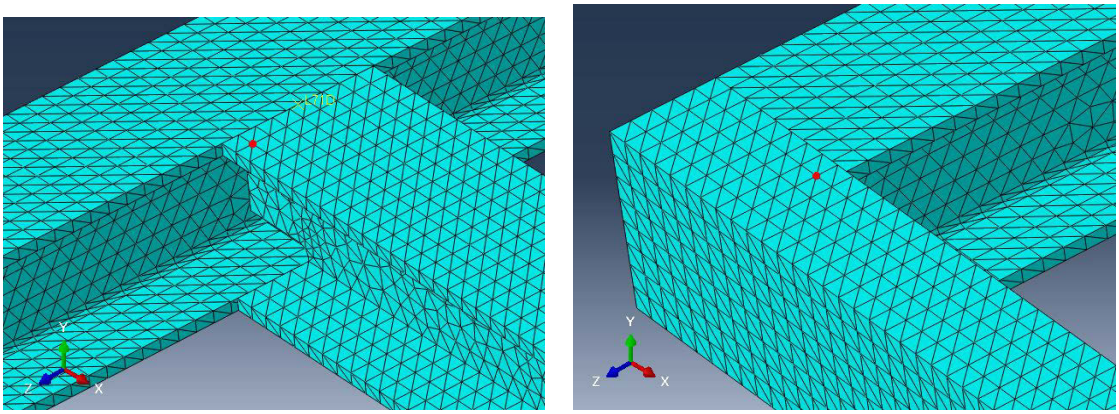

(a) T joint stress node (b) Corner joint stress node

Fig. 3.8: Nodes selected for stress analysis

These nodes were selected since they are the most reliable nodes nearest to the location of cracking as seen in the original cracked steel platform samples. The stress output from these nodes is plotted in Fig. 3.9.

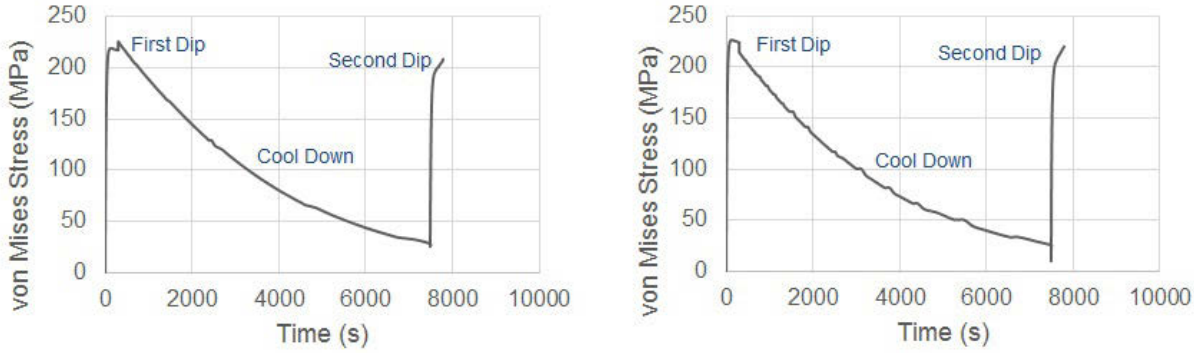

(a) Corner joint stress history (b) T joint stress history

Fig. 3.9: Stress at the crack locations during galvanizing by the FEA model

The plots show the expected stress profile from a double dip galvanizing process. The corner joint node reaches a peak stress of 226 MPa while the T-joint node reached a peak stress of 225 MPa. These stresses are significantly large and could obviously be the driving force for crack propagation. However, the stresses are not within the possibility of exceeding the yield strength of the material. This supports the notion that an embrittlement mechanism must have been present to cause the cracking in the steel platform structures. Another point worthy to note

is the stresses of hoisting the platform proved minuscule in comparison to the thermal stresses. The stress of hoisting reached approximately 10 MPa in the corner joint, which accounts for 4.5% of the 226 MPa peak stress value shown in Fig. 3.9. To further investigate the role of the thermal stresses, a contour plot of the stress distribution was applied to the model with a deformation scale factor of one. At the instant of peak stress, the stress distribution across the model is captured. The entire model with the contour plot is seen in Fig. 3.10.

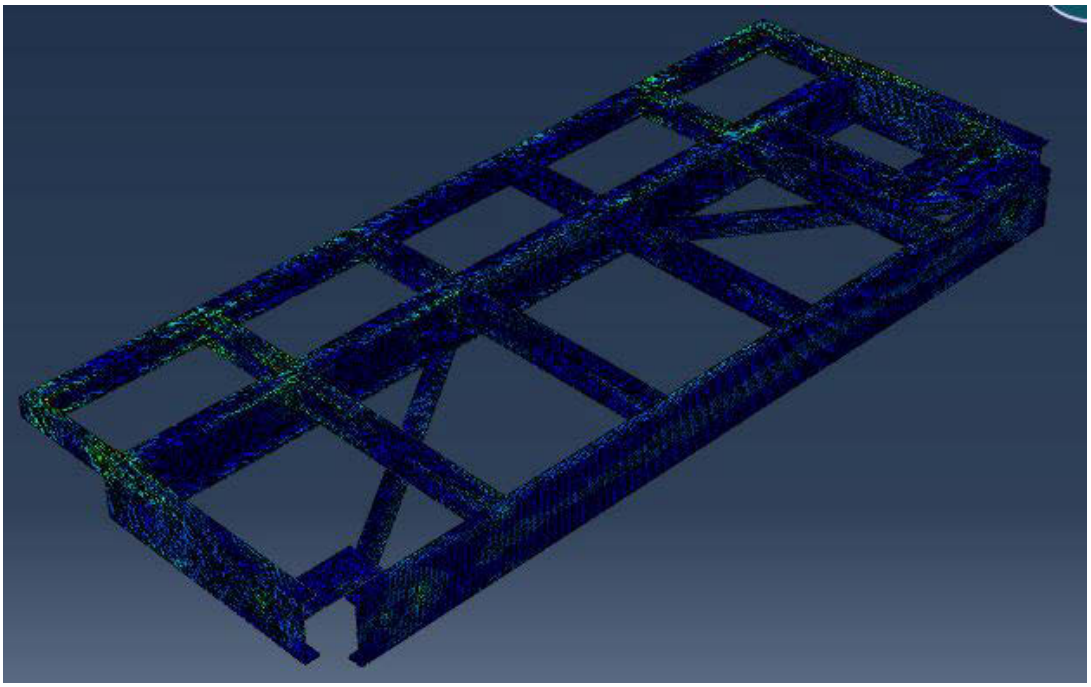

Fig. 3.10: Contour stress plot of the entire model

The image shows the stress is mainly concentrated in the beams that are submerged in the galvanizing bath and their connections. Fig. 3.10 gives an idea of the stress distribution across the entire model, but for the area of interest a more magnified view is needed to get the exact stress distribution at the joints, and to determine if it matches the cracking that was found. The detailed contour images during peak stress along with an image of the actual crack locations is given in Fig. 3.11 and Fig. 3.12.

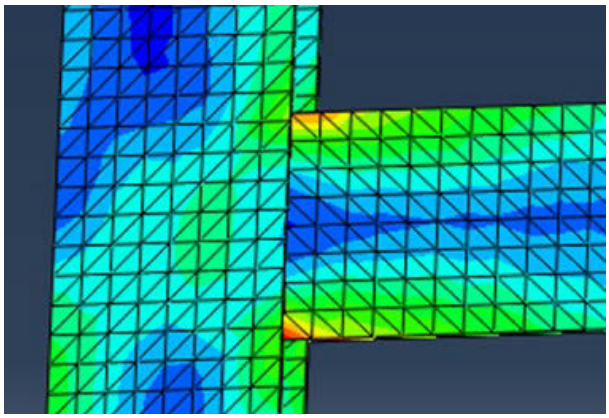

(a) T joint stress distribution

(b) T joint crack

Fig. 3.11: T-joint stress distribution and actual crack location

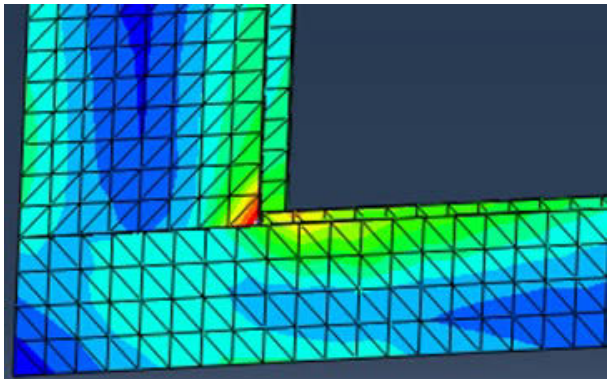

(a) Corner joint stress distribution

(b) Corner joint crack

Fig. 3.12: Corner joint stress distribution and actual crack location

The images show a stress distribution that closely matches the shape of the actual crack. In a sense, this is a more significant result than the peak stress during the double dip process. With this stress distribution, it can be said the cracking was driven by the thermal stresses of the galvanizing process, and the residual stresses of fabrication did not play a significant role in crack propagation. However, even though the stress was induced by the thermal gradient of the double dip process, the stress distribution also depends on the geometry and design of the steel structure. The stress distribution could be manipulated by altering the design.

3.4. Conclusions

The FEA study of the double dip galvanizing process on the steel platforms provided valuable insight into the thermal stresses of the process. From the study it can be concluded that the

stresses reached a considerable magnitude but did not exceed the yield strength of the steel. In addition, the thermal stresses were the driving force for crack propagation.

Although this study did not directly build on the results of Chapter 2 and operated independently, it once again helped build the knowledge base and understanding of the problem and supported the conclusions of Chapter 2 by showing evidence that an embrittlement factor was needed for the cracking to occur. In the following two chapters of the thesis, the most common embrittlement types during hot-dip galvanizing will be explored and the steel's susceptibility will be tested by lab experiments.

4. Hydrogen Embrittlement Study

4.1. Introduction

Hydrogen embrittlement was first documented in 1875 by W. H. Johnson [32]. After immersing both iron and steel in acid, he noticed a change in the material's fracture toughness and ductility. However, he noted the change in mechanical properties was not permanent. He also noted frothing occurred on the embrittled fracture surfaces after moistening. Through a trial and error process he deduced that it was only the acids containing hydrogen that caused the embrittlement and it was in fact, due to the hydrogen and not the acid itself. However, after leaving samples in hydrogen gas no signs of embrittlement were found. Using an electrochemical charing process and water, it was determined that the hydrogen must be nascent and not elemental. It was also noted the embrittlement occurred mostly in higher strength steels [32]. To this day, the fundamental conclusions of Johnson hold true, despite the large amount of literature and research surrounding hydrogen embrittlement.

The introduction of hydrogen into the material is the beginning of hydrogen embrittlement. Once the material's surface is exposed to the hydrogen, the atoms begin to diffuse into the metal. There are two significant factors that can ease the diffusion of hydrogen into the metal, the first being concentration gradient and the second being temperature [33]. Both of these factors are common to all diffusion situations. However, the diffusivity of hydrogen is already relatively high in steels and most steels contain little to no hydrogen, so for this reason the elevated temperature is not a necessity for hydrogen to diffuse easily into steels. There are several manufacturing methods that can possibly introduce hydrogen into the material, including electroplating, phosphating, and most notably pickling [7, 9, 34–37]. Pickling baths are used prior to galvanizing to clean the material's surfaces of any oxides, stains, or inorganic contaminants.

There are three factors that must be present for a steel to be susceptible to hydrogen embrittlement. This includes, hydrogen content, stress, and a susceptible microstructure [38]. A susceptible microstructure typically refers to the presence of martinsite and moreover, a high hardness level. Although the exact relationship among the three factors is not fully understood, a hardness threshold is commonly used to determine a steel's susceptibility. It is reported that if a steel has a Vickers hardness (HV) reading of less than 300 it is not susceptible to hydrogen

embrittlement. The most conservative value for the hydrogen susceptibility range were found to be 275 HV [7, 9, 36, 39]. Therefore the first step to assessing a steel's susceptibility to hydrogen embrittlement is to study the its hardness.

Hydrogen embrittlement is commonly associated with hot dip galvanizing. This is due to the pickling process prior to being hot dipped, which contains a hydrogen chloride solution. This is an excellent opportunity for active, diffusible hydrogen to enter into the steel [7, 9, 34–37, 39, 40]. Pickling is a long standing culprit in causing hydrogen embrittlement, however coupled with the stresses of hot-dip galvanizing almost all of the factors to cause hydrogen embrittlement are present from the processing alone. However, studies showing hydrogen embrittlement during the galvanizing process are usually done with steels that fall within the susceptible hardness range. It would be very uncharacteristic for 350W or 300W steel to show hardness levels that high.

When relating hydrogen embrittlement back to the cracked steel platforms, it is reasonable to suspect this embrittlement type as the cause of cracking. Given the large amount of literature and research that suggests cracking during galvanizing is hydrogen related, it is an embrittlement type that must be tested and explored. Also, when reflecting back on results from Chapter 2, it was seen there were some irregularities with thicker-than-usual grain boundaries that contained carbides. This may act as a susceptible microstructure. For this reason, actual testing for hydrogen embrittlement by charging samples with hydrogen must be carried out. Hardness testing will also be done to check for any irregularities in the base material or weld that cause the material to be in the susceptible range. Hardness testing will also give an idea if liquid metal embrittlement is at play at all, even though no signs of zinc were found in the crack, as discussed in Chapter 2.

4.2. Experimental Setup

Given the hardness threshold for susceptibility to hydrogen embrittlement (along with LME [8, 25]) hardness testing was carried out on the weld cross sections, which included some of the base material outside of the weld zone. For the hardness testing, four samples were used and taken from four different welds. The samples were mounted and ground in the same fashion as the metallography samples discussed in Chapter 1. Vickers hardness was measured using a 0.3N force with a dwell time of 10 seconds, done with a Tukon 2500 automatic hardness mapper.

The orientation of the indentation points and the number of indentations is inputted in the software. In this case, the indentations are oriented in a straight line across the weld with most cases having 75 indentation points. The hardness reading and indentation number was then processed into a comprehensive plot.

An experimental procedure was developed to test the hydrogen embrittlement susceptibility of the base material and welds. The premise of the test is to mechanically test samples that were put through the pickling process in comparison to samples that were not pickled. Any difference in the fracture mode or the material's strength would indicate hydrogen does impact the material properties. For the mechanical testing and fracture a standard tension test procedure was selected. To accurately gather all the desired information four test cases were developed as summarized in Table 4.1. Samples of the base material and of the weld were sectioned from a T-joint and cut into standard sizes for tension testing according to ASTM A370 [41]. The general location of the samples is shown in Fig. 4.1.

Table 4.1: Test cases

Test Case	Description
1	Not pickled base material
2	Pickled base material
3	Not pickled weld
4	Pickled weld

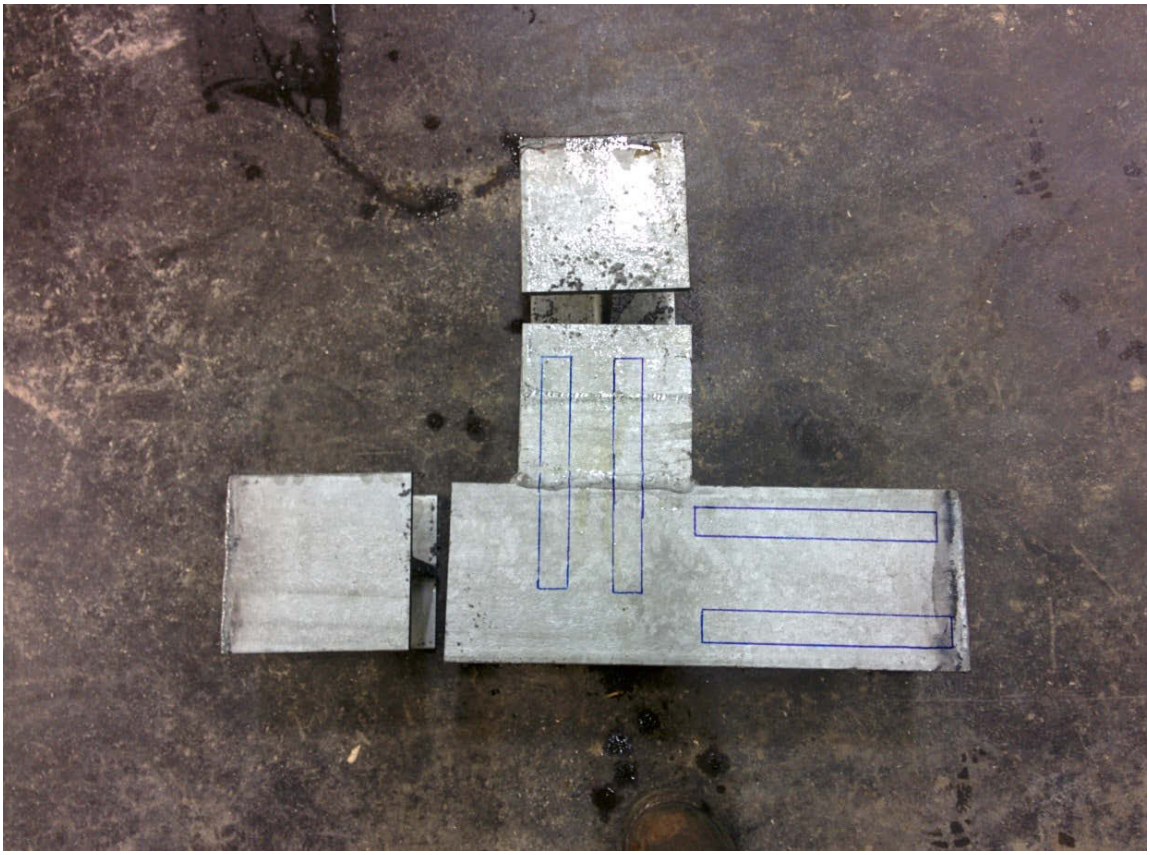

Fig. 4.1: Location of hydrogen embrittlement samples

The samples were transported to the same commercial galvanizing company that worked on the steel platforms. The tension samples were put through the same processing as the steel platforms except they did not get galvanized. However, they did undergo the pickling process to be charged with hydrogen. The pickling bath has a hydrogen chloride concentration of 13%. To prevent the hydrogen from diffusing out of the steel while being transported back to the lab, the samples were transported at -78.5°C in a polystyrene cooler filled with dry ice pellets. The tension tests were carried out with a strain rate of 0.25mm/min in the elastic region and 2.5mm/min in the plastic region until fracture occurred. The input force data was recorded along with the displacement data taken from a 1" gauge extensometer. The fracture mode, surfaces, and size of the ductile region would determine the potential presence of embrittlement (loss of ductility and fracture toughness).

4.3. Results and Discussion

4.3.1. Hardness Testing

The results of hardness testing across weld cross sections are shown in Fig. 4.2. Hardness values are measured in Vickers hardness (HV).

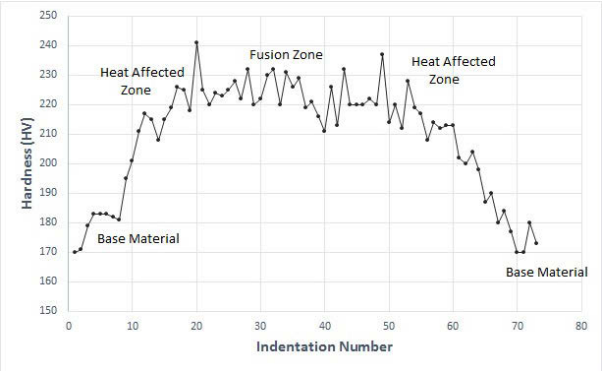

(a) Sample A

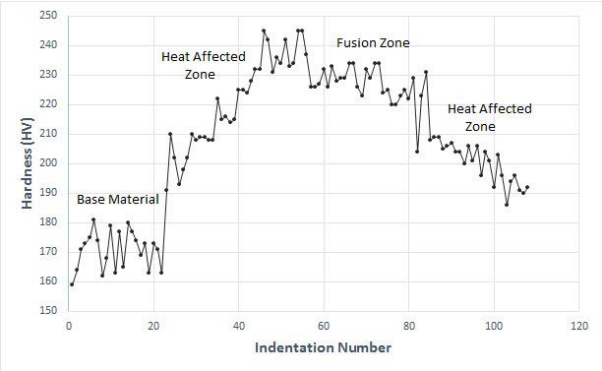

(b) Sample B

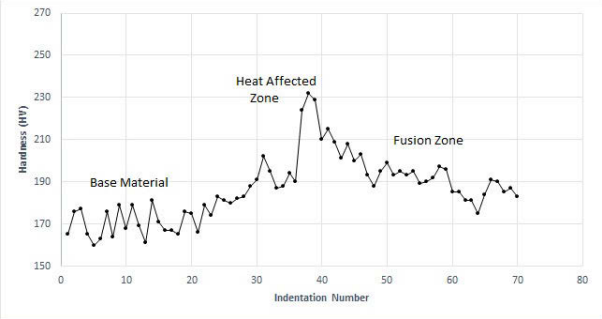

(c) Sample C

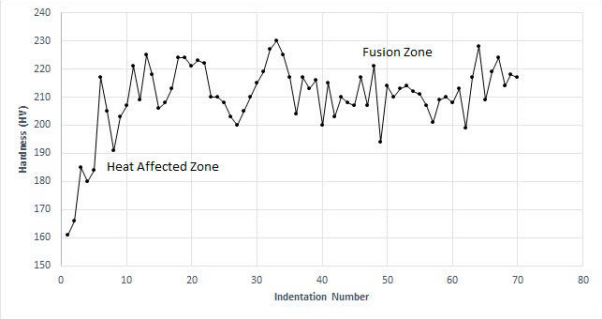

(d) Sample D

Fig. 4.2: Hardness measurements across weld cross sections

The hardness testing results all show an increase in hardness from the base material to the weld area. The most classic shape of hardness testing across a weld is seen in Fig. 4.2(a) with a rise and fall of the hardness values. Fig. 4.2(b) shows this shape somewhat as well, but the hardness does not drop off as steeply, possibly due to a larger heat affected zone. It is important to note that in neither case is the hardness of the heat affected zone larger than the hardness of the fusion zone. Fig. 4.2(c) and (d) however show a much more unusual shape. Fig. 4.2(c) shows a very gradual increase from the nominal base material value of 170 HV, so much so that it is almost not noticeable. However, there is a very noticeable spike in hardness at the center of the sample. But overall the weld hardness from this sample did not show the same increase in magnitude as the others. Finally, the sample in Fig. 4.2(d) shows similar values to the samples

in Fig. 4.2(a) and (b) and also the same large increase as the indentations move into the weld zone on the left side of the plot. The hardness does not drop on the right but this is likely due to hardness mapping not reaching outside the weld zone.

The most significant data from the hardness testing is the peak value. In Fig. 4.2(a), (b), (c), and (d) the maximum hardness readings are 241 HV, 245 HV, 232 HV, and 230 HV respectively. It is also important to note that the hardness of the base material consistently reads 170 - 180 HV. These values are expected for 350W and 300W steel along with their welds. Ultimately these results show that there is nothing irregular with the hardness levels of the material, which is supported by the typical pearlitic carbide structure seen in Chapter 2.

As previously noted, both LME and hydrogen embrittlement depend heavily on a susceptible microstructure which is measured by hardness testing. But even the peak hardness values in any region are very short of the minimum hardness values reported for susceptibility to LME and hydrogen cracking. Given these hardness results and the lack of zinc found in the mid-crack and near the crack arrest, LME is not a reasonable explanation for cracking. This also eliminates one of the three contributing factors for hydrogen embrittlement. This makes the notion of hydrogen cracking unlikely. It would be very unusual and perhaps even extraordinary to discover hydrogen cracking in a case with such low hardness. But the considerable stresses induced by the double dip galvanizing process must still be considered, along with the hydrogen that is charged into the material during pickling. Further investigation into hydrogen embrittlement is warranted.

4.3.2. Tension Testing

Despite the results of the hardness testing, the experimental study on hydrogen embrittlement was still carried out through tension testing. The fracture surfaces of the tension tests with hydrogen-charged samples is shown in Fig. 4.3. Fig. 4.3(a) and (b) shows the fracture surface of the base material sample not pickled and pickled. Similarly, Fig. 4.3(b) and (c) show the sample across the weld pickled and not pickled. It should also be noted that in Fig. 4.3(c) and (d) the fracture did not occur in the weld, but in the base material.

(a) Base material, not pickled

(b) Base material, pickled

(c) Across weld, not pickled

(d) Across weld, pickled

Fig. 4.3: Fracture surfaces of hydrogen-charged samples

The main purpose of this experiment is to compare the fracture surface of the samples that were pickled against the samples that were not. However, a visual inspection of all four samples fracture surfaces shows no significant difference. Similar features are found on each surface and more significantly they all share ductile features. Evidence of ductile fracture is shown by the cup and cone features and plastic deformation. The pickling process and introduction of hydrogen into the steel had no impact on the mechanical properties. Overall it can be said there is no difference in fracture mode among the different samples.

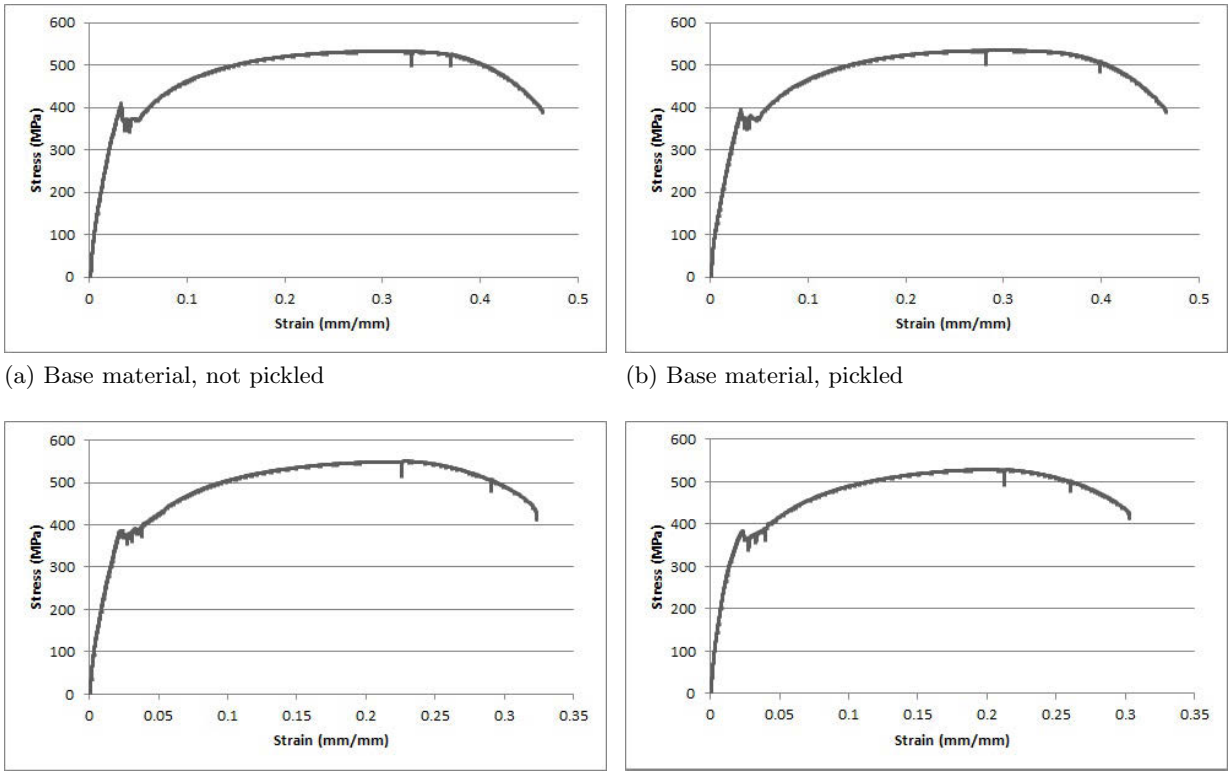

(a) Base material, not pickled

(b) Base material, pickled

(c) Across weld, not pickled

(d) Across weld, pickled

Fig. 4.4: Tension test results of hydrogen-charged samples

To support the discussion of the visual inspection of the fracture surface, the data from the tension tests were also analyzed. The numerical stress–strain data from the tension testing is graphically shown in Fig. 4.4 for each different type of sample, which includes the pickled base material and weld samples, and the unpickled base material and weld samples. The images show no change between the samples that were pickled and the samples that were not. The ductile behavior is the same with both types of samples showing a large plastic region and necking before the final fracture. The only difference between the samples is the welded samples did not have as large a plastic region as the base material samples, since they did not experience as

much strain before fracture. This is an interesting result since the welded samples both broke in the base material. In any case, all the graphs show the typical behavior of an elastic region and large plastic region, meaning deformation along with necking and ductile fracture. It appears the pickling process and introduction of hydrogen into the steel or welds has no effect on the material's fracture toughness or tensile behavior.

From the results of Chapters 2 and 3 it is seen that an embrittlement mechanism is needed for the material to crack in the brittle manner that occurred during galvanizing. However the results of this chapter conclude that it was not a case of hydrogen embrittlement. The pickling process does allow for hydrogen to diffuse into steel, however the material is not susceptible. Although hydrogen embrittlement can be removed from the list of possible factors, this does not determine the cause of cracking. Literature has also stated that temper embrittlement may be a possibility, which is the next logical study to conduct.

4.4. Conclusions

Hardness testing of the base material and welds, along with tension testing of pickled samples, was used determine to the material's susceptibility to hydrogen embrittlement. The results of the hardness testing were compared to the values reported in literature to determine susceptibility. The results from the tension testing of the pickled samples were compared to those of regular samples. The tension testing determined if the hydrogen introduced into the steel during pickling had any impact on the mechanical properties.

From the results of the hardness testing, the steel platform's base material and welds are not within the range of susceptibility. This leads to the conclusion that hydrogen embrittlement was not the mechanism that caused cracking in the steel platform structures. As one of the three factors needed is not present. The hardness testing results from this chapter and the lack of zinc seen in the fractography study in Chapter 2 both indicate the LME can be eliminated as a possible cause for cracking as well.

The fracture surfaces of the tension testing all showed signs of ductile fracture and no resemblance to the fracture surfaces of the cracked samples. Charging the samples with hydrogen and fracturing them failed to recreate the fracture surface from the galvanizing cracking, and moreover the fracture surfaces of the pickling samples matched the ductile surfaces of the unpickled

samples. Once again the material exhibited ductile behavior instead of the brittle behavior seen from the original incident of cracking. From these tests, in conjunction with the results of the hardness testing, it can be stated that hydrogen embrittlement was not the cause of cracking in the steel frames and can be eliminated as an option.

5. Temper Embrittlement Study

5.1. Introduction

Temper embrittlement is traditionally used to describe an embrittlement phenomenon during the tempering of quenched steels. Temper embrittlement typically occurs while aging a steel through a susceptible temperature range, or when slowly cooling steel through that range. For carbon steel, this range is 370 °C – 560 °C [7, 10, 19, 20, 22]. Recent research using AES has shown that the exact mechanism of embrittlement is a migration of impurities to the grain boundaries [42, 43]. The impurity-rich grain boundaries cause a weakness in the structure. This results in a decrease in the material's ductility and fracture toughness [21, 23, 24, 44, 45]. The main element to cause weakness in the grain boundaries is phosphorus, however elements such as nickel, chromium, and manganese promote the segregation of impurities to the grain boundary [10, 19–23]. When evaluating the susceptibility of a material and process to temper embrittlement, the two main factors to consider are the chemistry of the material (if the culprit elements are present) and if the process temperature is within the susceptible range.

Temper embrittlement has been reported in a few incidents of galvanizing. However, because it is not a tempering process, it is sometimes given a different name. Overall it is the same mechanism of embrittlement. The galvanizing bath sits at approximately 450 °C, which is within the temper embrittlement range [10, 22]. It should also be noted that the galvanized parts or structures cool slowly from 450 °C, which for some portion, falls within the temper embrittlement range. The embrittlement is not related to the molten zinc or galvanizing process directly, but rather the heating cycle and thermal stresses make temper embrittlement a concern [22]. This is particularly relevant in the case of a double dipping process, where the thermal gradient across the structure is large, which creates significant thermal stresses in the structure. The main factor influencing susceptibility to temper embrittlement during galvanizing is the material's chemistry. The external factors are all provided by the galvanizing process.

The cracking that occurred in the steel platforms may be related to the mechanisms of temper embrittlement, especially after the EDS results seen in Chapter 2. EDS line scans consistently showed spikes in phosphorus content in the grain boundary. Manganese and carbon spikes were found as well. All of this makes a temper embrittlement study beneficial. The first

step in the study is to conduct a compositional analysis of the material. Under the G40.21 specifications set for Canadian structural steel, there should be no cause for concern of temper embrittlement. However, under the right balance of elements temper embrittlement can still occur. The composition of the base material along with the steel mill's chemistry reports will show if there is anything out of the ordinary in the steel. Secondly, an experiment can be developed to try to recreate the fracture surface found in the original cracks. This should be similar to the hydrogen embrittlement tension testing done in Chapter 4. The fracture surface is once again the result of interest and studied for similarities or differences to the original surfaces. Lastly, a review and minor study of the diffusivity of phosphorus in steel can show the mobility of the phosphorous in steel during galvanizing.

5.2. Experimental Setup

The cornerstone of temper embrittlement susceptibility is the material's chemistry. Two methods of composition analysis were used in this study, X-ray florescence (XRF) and optical emission spectroscopy (OES). For the XRF analysis three samples were used, and tested on 3 different locations per sample. Similarly, for the OES three samples were used which were taken from the center of the base material's thickness. Along with the measured composition analysis, the mill chemistry reports for select beams of interest were gathered. It is unknown exactly how the mills tested the material's composition.

XRF operates on a similar principle to EDS in that the sample is excited to cause the release of a lower level electron and a higher level electron to fill the hole. The energy or radiation released during this ionization is matched with it's atomic characteristic. However the major difference comes into play during the excitation process. XRF uses a secondary target that is excited by the source, but the florescence given off from exciting the secondary target then excites the sample [46]. This is in contrast to the direct excitation of EDS. Another difference with regards to the excitation is that unlike EDS, XRF does not use a high energy electron beam for the excitation. Rather, a photon source is used, which is more bulk sensitive than using a high energy electron beam source and EDS.

OES operates by applying electrical energy, in various forms, to the sample and vaporizing the atoms. The vaporized atoms form a discharged plasma and the atoms are brought to a high energy state. A unique spectrum discharge is produced, which is matched to its uniquely

corresponding element. What is exactly measured is the light given off during the heating of the sample. The light goes through a diffraction grating which extracts the exact emission spectrum to the detectors. The detectors read for which spectrum are present and the intensity corresponds to the concentration of the element [47].

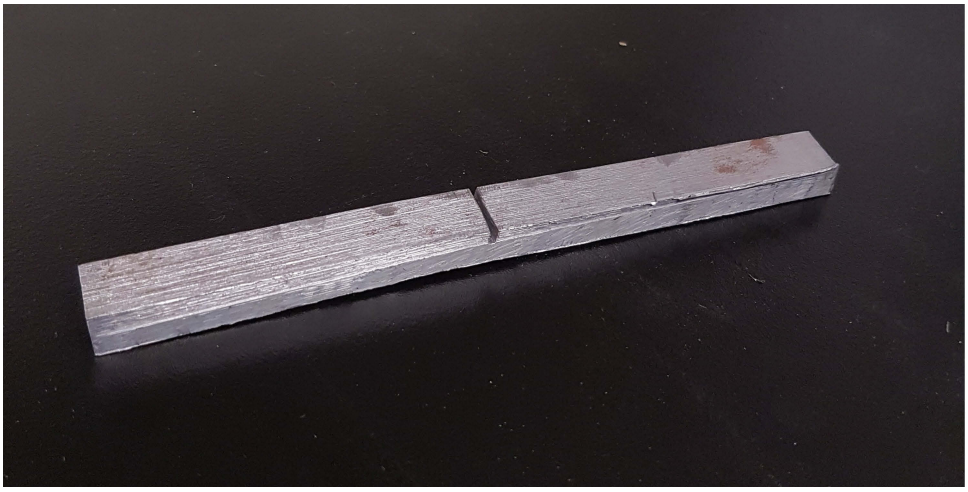

Fig. 5.1: Temper Embrittlement Sample

In an attempt to recreate the fracture mode from the galvanizing cracks, an original experimental test was developed. The focus of the test is to fracture the sample at an elevated temperature. Samples were sectioned from the provided joints and cut to dimensions of approximately 10mm x 150mm x 150mm. An image of a sample is shown in Fig. 5.1. A notch of half the sample's thickness was put at the center of the sample's length. The purpose of the notch is to create a location for fracture to occur, and the reduction in cross section will also allow the fracture to occur more easily. Six samples were prepared and tested. The samples were heated to 450°C and then fractured. Using the lumped capacitance method, the heating time for the sample to reach 450°C was determined as:

$$t = \frac{-\rho V C_p}{h A_s} \ln\left(\frac{T_i - T_f}{T - T_f}\right) \tag{5.1}$$

In this equation ρ, V, and C_p are the sample's density, volume and specific heat capacity, respectively. h refers to the convection coefficient in the heating process and A_s is the sample's surface area. Lastly, T_i is the sample's initial temperature and T_f is the temperature of the furnace. T_f was manipulated to get a desired heating time. The temperature of the sample was confirmed with the use of a touch thermocouple.

The fracture was created by supporting the sample on both of its ends, with the notch facing downwards. An impact force, created by a chisel and hammer, was applied to the side opposite of the notch. This is a similar test set up to a 3-point bend test, but an impact force was applied in a fashion similar to Charpy impact testing. However, in the end the result of interest is the fracture surface, since the test objective is to determine if the elevated temperature causes a brittle fracture. Thus, as long as a fracture surface is produced the results of the test can be analyzed. The fracture surfaces were analyzed by SEM as well as visually.

5.3. Results and Discussion

All of the compositional analysis of the base material along with the chemistry specifications in accordance to the G40.21 standards are summarized in Table 5.1. The steel mill's chemistry report data was provided for several beams used in the steel structure. According to the G40.21 structural steel chemistry standards, the beams are within specification [48]. To confirm the analysis of the steel mill, an XRF study was done on three different samples and three different locations per sample. The results shown from the XRF analysis in Table 5.1 are fairly different from the values reported by the steel mill. Most obviously is the aluminum, and perhaps more significantly the sulfur content. The specification for sulfur content is 0.05 wt% maximum [48] and a sulfur content of 0.228 wt% is very uncharacteristic for structural steel and questionable. To gather more data along with the XRF readings, an OES analysis was carried about on three samples. Given the accepted accuracy of OES for trace elements [49] and the closeness to the values of the steel mill reports, the OES readings are taken as the most accurate. However, it should be noted the high phosphorus content reported by the OES, which is slightly out of the specification of 0.04 wt% maximum [48]. The steel mill reports show a relatively high phosphorus content as well, but not quite as high and not outside of the specification. It should be noted that phosphorus is a key culprit in susceptibility to temper embrittlement. In addition to phosphorus, elements such as silicon and manganese create susceptibility to temper embrittlement, which are both shown to be present within the susceptible range [34]. The results of the composition study show a susceptibility to temper embrittlement. However, if the results of the XRF analysis are true, this leaves the steel susceptible to hot short [50]. In either case, the results point towards a type of embrittlement that is temperature activated.

To explore the notion of grain boundary segregation, the bulk diffusivity of elements of interest

Table 5.1: Compositional analysis

Element	Wt% Mill Report	Wt% OES	Wt% XRF	Wt% G40.21
C	0.18	0.19	N/A	0.23 max
Al	0.006	0.015	1.212	N/A
Si	0.150	0.237	0.612	0.40 max
S	0.018	0.017	0.228	0.05 max
Cr	N/A	0.164	0.242	N/A
Mn	0.610	0.655	0.647	0.50–1.50
Cu	0.300	0.305	0.292	N/A
Zn	N/A	N/A	0.702	N/A
P	0.033	0.042	N/A	0.04 max
Ni	0.100	0.091	N/A	N/A
Sn	N/A	0.016	N/A	N/A

in ferrite can be compared, using values for the activation energy and maximal diffusion found in literature [51, 52]. Table 5.2 shows the diffusivity of each element at 450 °C. It is important to note that carbon has the highest diffusivity, which explains the large amount of carbon segregation found in Fig. 2.6. However, following carbon is phosphorus and sulfur. Given the heating, cooling and stress cycle that occurred in the steel structure, it is likely that phosphorus would have diffused in a similar way to carbon.

Table 5.2: Element Diffusivity

Element	Diffusivity (m^2/s)
H	3.125×10^{-5}
C	1.384×10^{-8}
P	5.442×10^{-16}
S	8.55×10^{-16}
Si	4.598×10^{-18}
Mn	2.734×10^{-17}

In a separate study carried out, it was found that phosphorus grain boundary diffusion occurs more easily than bulk diffusion. Using AES techniques the study determined an experimental diffusivity for phosphorus and the presence of phosphorus in the grain boundaries after exposure to a similar temperature range [43].

The fracture surfaces of four different samples from the temper embrittlement test are shown in Fig. 5.2. Samples were taken from two different beams and are composed of purely base material. All of the samples broke in a similar fashion, with sudden fracture and typically with only one or two strikes with the hammer and chisel. There was minimal bending of the sample

during fracture and some of the surfaces turned blue upon fracture, which is thought to be the oxidation of the grain boundaries. Each fracture surface shows relatively flat features and does not show signs of multiple cracks. In contrast to the hydrogen embrittlement samples, there is no stretching of the material and no cup and cone like features. Overall it seems there are signs of ductile fracture, and rather the features of the surface point towards brittle fracture. The surfaces of these samples more closely resemble the original fracture surface samples. However, it is much more telling if the samples are observed microscopically and then compared to the original crack surfaces.

(a) Sample A

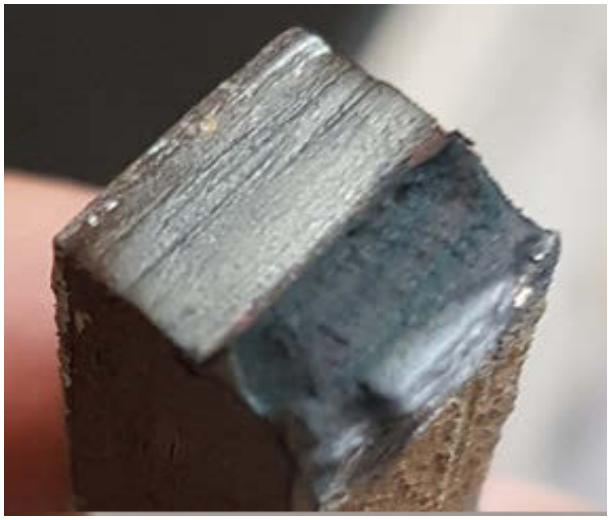

(b) Sample B

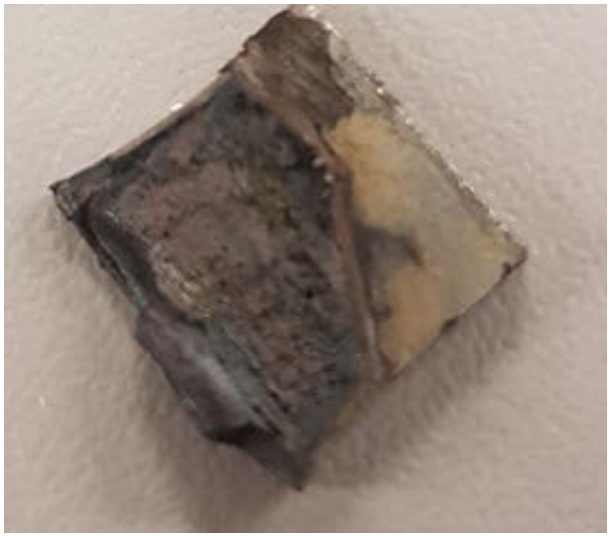

(c) Sample C

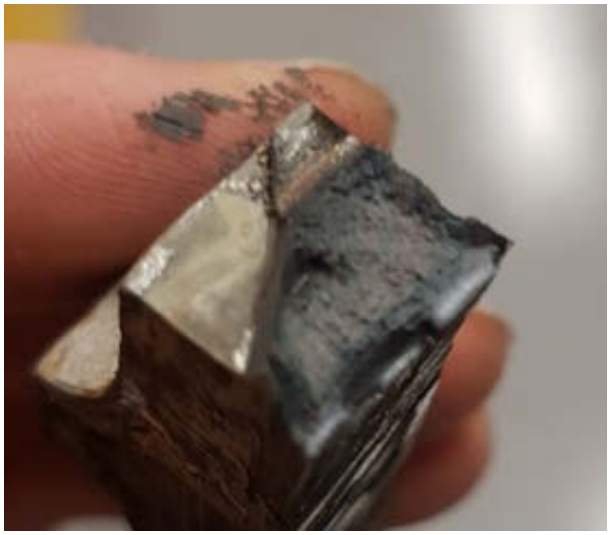

(d) Sample D

Fig. 5.2: Fracture surfaces of temper embrittlement test

The fracture surfaces from the temper embrittlement testing were also observed under the SEM.

In Fig. 5.3(b) and (d) the images of the lab sample fracture surface are shown at 200X and 500X respectively. The lab surfaces show the same features, grain boundary separation and similar dimple sizes as the received fracture surfaces. Fig. 5.3(a) and (c) give a comparison to the provided sample's fracture surfaces from Fig. 2.14. The similarities between the two fractures is stunning. The only noticeable difference in the images is that in Fig. 5.3(d) there are a few microvoids present, which seem to all be along the grain edges.

Similarly, in Fig. 5.4 a comparison is shown of the ambient lab fracture sample in Fig. 5.4(a) and the temper embrittlement testing fracture sample in Fig. 5.4(b). Both images are shown at 500X. The difference in the deformation of the surface is apparent as there are many microvoids and the grain boundaries are not recognizable in Fig. 5.4(a). The obvious differences in this comparison also reinforces the idea of how stark the similarities are between the surfaces in Fig. 5.3. For the same material to behave so differently under different temperature conditions is a key finding. The similarities and differences between the comparisons shows that the original fracture is recreated by elevated temperature fracture. The increase in the material's temperature clearly has an impact on its fracture toughness, thought to be caused by the diffusion of phosphorus and other impurities to the grain boundaries. Overall, the temper embrittlement testing proved a temperature activated embrittlement mechanism is present.

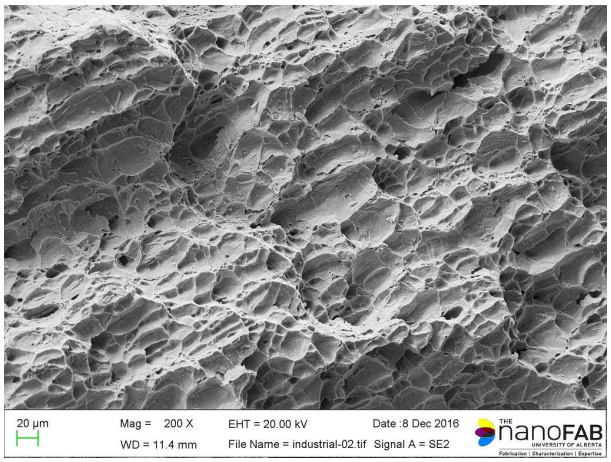

(a) Received surface 200X

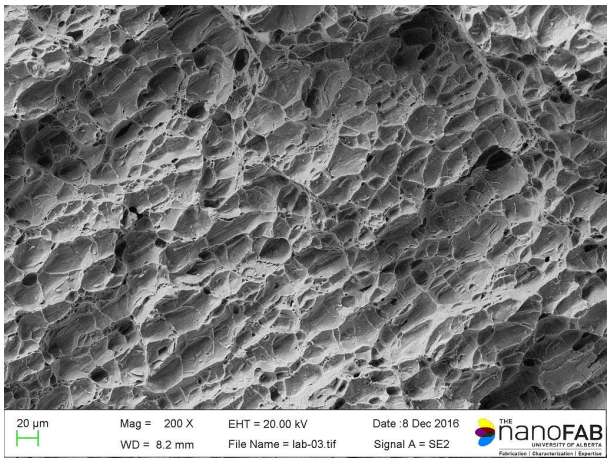

(b) Lab surface 200X

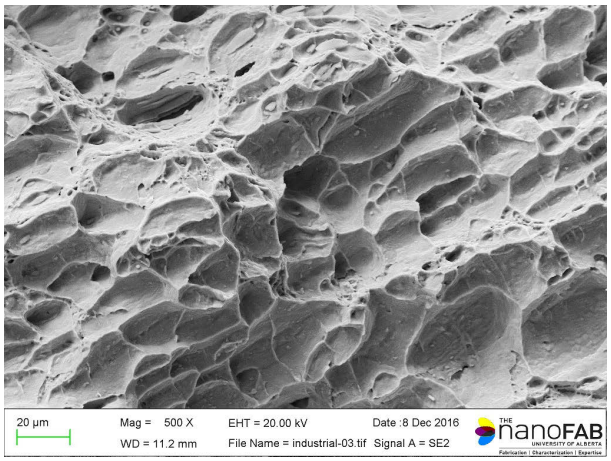

(c) Received surface 500X

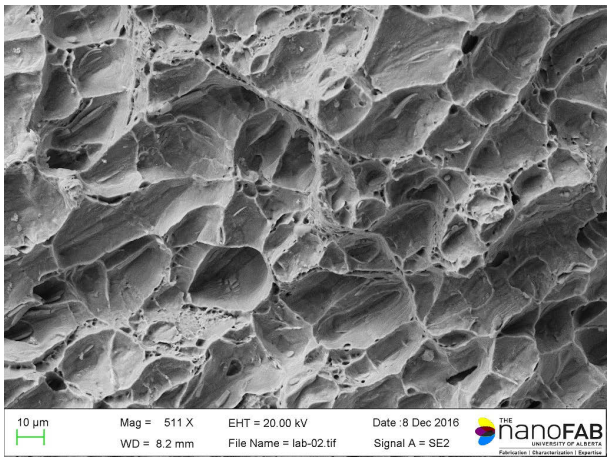

(d) Lab surface 500X

Fig. 5.3: Comparison of 200X & 500X SEM images of the received fracture surface and lab fracture surface

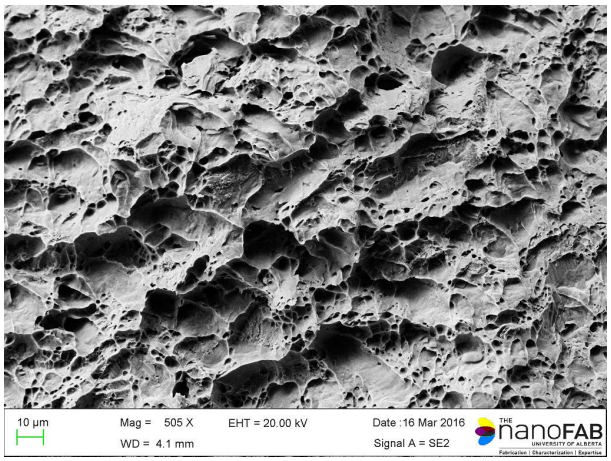

(a) Ambient temperature fracture surface

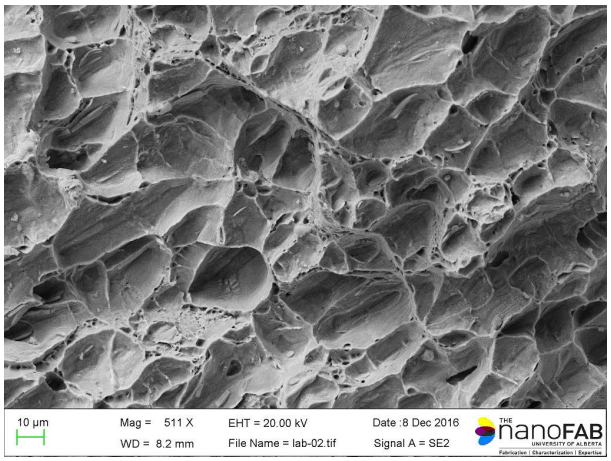

(b) Elevated temperature fracture surface

Fig. 5.4: Comparison of 500X SEM images of the ambient fracture surface and galvanizing temperature fracture surface

Chemical composition and elevated temperature fracture testing, along with a study on the diffusivity of different elements in ferritic steel was used to investigate the notion of temper embrittlement susceptibility in the steel. The results of the chemical composition testing showed unusually high levels of phosphorus, relative to the Canadian standards. The phosphorus content along with the low diffusivity and tendency for phosphorus to diffuse to the grain boundaries agree with the EDS scans of Chapter 2. The results of the elevated temperature fracture testing showed vastly different results from the ambient fracture testing. It also showed a different fracture surface features compared to what was seen in the hydrogen embrittlement testing

5.4. Conclusions

The definitive conclusion that can be drawn from the chemical composition analysis is that phosphorous content is higher than what is acceptable. The mill test reports show high phosphorous content and the OES testing shows a phosphorous weight percentage outside the chemistry standards. The presence of phosphorous in the grain boundaries is strongly supported with the EDS scans of Chapter 2 and the diffusivity coefficients explored in this chapter.

The brittle fracture results of the elevated temperature testing confirmed that embrittlement is activated by the exposure to the heat of the galvanizing bath. Given that the fracture surface of the original cracks could not be reproduced until the elevated temperature testing, and the fracture surfaces of the elevated temperature test samples closely matched, it can be concluded that the embrittlement mechanism is temperature activated and can be considered a type of temper embrittlement. Even though there is strong evidence to suggest phosphorus was the critical impurity in the steel, further study could be completed to explore its role.

With the conclusions of this chapter, a final overall project conclusion can be reached. With the elimination of hydrogen embrittlement as a failure mechanism, along with the successful results of this chapter an explanation for the cracking of the steel platforms can be proposed. Furthermore, this project also opens many doors to explore temper embrittlement mechanisms during galvanizing, particularly with regards to 350W and 300W steel.

6. Conclusions and Future Work

6.1. Conclusions and Summary Findings

Using the twelve cracked samples provided by the industry partner, an extensive study of the material's metallurgy and fracture surface was done. The most significant finding across the whole study may have been the lack of ductile features on the fracture surface. The crack appeared brittle which is uncharacteristic for 350W and 300W steel. Even more interestingly, the brittle fracture could not be recreated in the lab. Each attempt showed a typical ductile fracture, without any of the features from the provided sample. However, on the metallurgy side of the study, another significant finding was the thicker grain boundaries containing impurities and carbides. EDS scans found the grain boundaries were rich in carbon, phosphorus and in some cases manganese as well. This discovery shaped the next steps of this research project and thesis. Altogether though, the microstructure of the base material and weld was as expected, showing ferrite grains and a pearlitic carbide structure.

An FEA study to model the galvanizing process had several benefits. The FEA was able to put metrics to the thermal stresses of the double dip process. The stresses showed a considerable load on the structures joints, however they were not enough to surpass the yield strength of the material. For failure to occur, an embrittlement mechanism would be needed to weaken the material. The stress distribution also showed the highest stresses occurring in the joints that experienced cracking, and the shape of the distribution matched the shape and orientation of the cracks. From this another major conclusion can be drawn: the thermal stresses of the galvanizing process were the driving force for crack propagation.

Given the results of the metallography, fractography, and the FEA, two experimental studies were done to evaluate the material's susceptibility. Given the history and commonly reported incidents of hydrogen embrittlement it was studied first. The hardness testing showed nothing abnormal in the base material or in the weld zone, with relatively low readings in comparison to steels where hydrogen embrittlement usually occurs. The hardness of the samples was outside the specified range for hydrogen embrittlement, but in the case the material still had a susceptibility a further experimental test was done. The samples were charged with hydrogen and fractured, however the fractures of the samples with hydrogen had the same behavior and

features as the regular samples. The hydrogen did not affect the mechanical properties of base material or weld and therefore, hydrogen embrittlement can be eliminated as a possible cause of cracking.

In a similar fashion, an experimental study was done on temper embrittlement susceptibility. First, the chemical composition of the material was studied using two different analysis methods and by reviewing the data given by the steel mill. Phosphorus was found to be relatively high while the other elements were all well within the material's chemical specification. However, it should also be noted that certain elements such as manganese were measured within required range for temper embrittlement. Overall from the compositional analysis, it can be concluded the material shows signs of susceptibility to temper embrittlement. To determine the impact an elevated temperature has on the material's mechanical properties, samples were heated to the galvanizing temperature and fractured. Unlike previous fractures, the surface from the elevated temperature testing showed features resembling the provided sample's cracks. The definitive conclusion that can be drawn from this study, is that the elevated temperature has a negative impact on the material's fracture toughness and ductility. Given the evidence for temper embrittlement, such as high phosphorus content and grain boundary segregation, it is beyond a reasonable doubt that it was the embrittlement mechanism that lead to cracking in the steel platform structure.

The studies performed in this project all built on each other to reach a final conclusion. To ensure consistency in the test results all the testing and analysis was done exclusively on the steel that was used to construct the steel platforms. The steel metallurgy, chemical composition, and mechanical behavior in difference circumstances were all used to showcase that a temperature activated embrittlement mechanism was the cause of cracking. The findings of this thesis contribute valuable knowledge in the area of cracking during galvanizing, and may prompt further study of temper embrittlement cases during galvanizing.

For the industry parter, there are several options for developing a mitigation plan. When dealing with an elevated temperature process, such as double dip galvanizing, the elements of temper embrittlement (especially phosphorus) should be given extra consideration. Although it would be unreasonable to perform OES on top of every MTR, the MTRs should be examined closely for not only higher content elements, but the combination of culprit elements in high amounts.

Another approach may be to redesign the structure to manipulate the stress distribution and reduce the stress concentrations. Without the driving force to cause crack initiation or propagation, the cracking would not occur. In addition, if it is possible, eliminating the double dip process for a complete submersion of the structure would get rid of the thermal gradient, and thus the thermal stresses. Finally, and perhaps the most difficult to implement, if the diffusivity of the impurities could be reduced they would not be able to segregate to the grain boundaries. For example, the addition of molybdenum to the steel inhibits phosphorus' diffusivity Without elements such as phosphorus in the grain boundaries the fracture toughness and ductility of the material would not be affected.

6.2. Future Work

- The diffusion of phosphorus in ferritic steel was briefly covered in this thesis. However further research and experimental study would greatly benefit the field of temper embrittlement. A study on the diffusivity of phosphorus-rich mild steel during galvanizing would be an excellent contribution to knowledge base of cracks related to galvanizing.
- Since temper embrittlement commonly occurs in alloyed steels, many susceptibility tests and equations exist only for those steels. Temper embrittlement occurring in mild steel with impurities could be expanded by developing a governing equation for susceptibility.
- Although an elevated temperature fracture test was conducted in this thesis, the test did not have any data acquisition. This experiment could be expanded to further to collect metrics on the impact force that caused the fracture in the samples. Furthermore, this test could be modified to heat the sample for a tension test as opposed to an impact test. The material's tensile behavior could then be analyzed and compared to the ambient tensile behavior and properties.

7. References

[1] American Galvanizers Association (2011). What is Hot-Dip Galvanizing (HDG)?

[2] Metal Supermarkets (2014). Galvanizing: Why is it important?

[3] Metal Supermarkets (2016). What is Galvanizing?

[4] Francis, P. E. (19). Cathodic Protection in Practise. *NPL Report*, 1–22.

[5] American Galvanizers Association (2009). HGD Process.

[6] Shibli, S. M. A., B. N. Meena, and R. Remya (2015). A review on recent approaches in the field of hot dip zinc galvanizing process. *Surface and Coatings Technology 262*, 210–215.

[7] AZoM (2003). Galvanised Steel Embrittlement Due to Hot Dip Galvanising. pp. 1–4.

[8] James, N. (2009). Designing against LMAC in galvanised steel structures. *Engineering Failure Analysis 16*(4), 1051–1061.

[9] Mraz, L. and J. Lesay (2009). Problems with reliability and safety of hot dip galvanized steel structures. *Soldagem & Inspeção (Impresso) 14*(2), 184–190.

[10] Panzenböck, M. and P. Schütz (2014). Embrittlement of Mild Steels during Hot Dip Galvanization. *Microscopy and Microanalysis 20*(S3), 1868–1869.

[11] Diez, D. (2013). Metallography - an Introduction.

[12] Parrington, R. J. (2002). ractography is critical to failure analysis of metals and plastics . Fractography of plastics is a rel-. *Practical Failure Analysis 2*(October), 33–38.

[13] Anderson, T. L. (2005). *Fracture Mechanics Fundamentals and Applications* (Third ed.). Boca Raton, FL: Taylor and Francis.

[14] University of California (2015). Introduction to Energy Dispersive X-ray Spectrometry (EDS). pp. 1–12.

[15] Barthes-Labrousse, M.-G. (1995). The Auger Effect. *Microsc. Microanal. Microsruct 6*(June), 253–262.

[16] Li, L. and R. Messler (2002). Segregation of Phosphorus and Sulfur in Heat-Affected Zone Hot Cracking of Type 308 Stainless Steel. *Welding Journal* (May), 78–84.

[17] White, C. L., S. A. David, and M. W. Richey (1987). Application of Auger Electron Spectroscopy to the Study of Trace Element Effects on Weldability. In J. Y. Koo (Ed.), *Welding Metallurgy of Structural Steels*, Denver, CO, pp. 101 – 114. The Metallurgical Society, Inc.

[18] Youn, J. G. and K. H. J. (1987). Characteristics of TMCP Steel and its Softening. In J. Y. Koo (Ed.), *Welding Metallurgy of Structural Steels*, Denver, CO, pp. 157 – 168. The Metallurgical Society, Inc.

[19] Materia, T. (2003). Temper Embrittlement.

[20] TWI (2010). What is temper embrittlement, and how can it be controlled?

[21] Yu, J. and C. J. McMahon (1980). The effects of composition and carbide precipitation on temper embrittlement of 2.25 Cr-1 Mo steel: Part II. Effects of Mn and Si. *Metallurgical Transactions A 11*(2), 291–300.

[22] SorelMetal (1999). *Ductile Iron Data for Design Engineers*. Montreal, QC: Rio Tinto Iron & Titanium Inc.

[23] Mulford, R. A., C. J. Mcmahon, D. P. Pope, and H. C. Feng (1976). Temper embrittlement of Ni-Cr Steels by phosphorus. *Metallurgical Transactions A 7*(7), 1183–1195.

[24] Kim, G. S., J. E. Indacochea, and T. D. Spry (1987). Weldability Studies in Cr-Mo-V Turbine Rotor Steel. In J. Y. Koo (Ed.), *Welding Metallurgy of Structural Steels*, Denver, CO, pp. 79 – 100. The Metallurgical Society, Inc.

[25] Kikuta, Y., T. Araki, and M. Yoneda (1986). Liquid Metal Embrittlement Cracking By Molten Zinc Structural Steel HAZ. Technical report, Oksaka University.

[26] Thomee, V. (2006). *Galerkin Finite Element Methods for Parabolic Problems* (Second ed.). Berlin: Springer.

[27] Szabo, B. and I. Babuska (1991). *Finite Element Analysis* (First ed.). New York, NY: John Wiley & Sons.

[28] Niazy, A. M. (1997). Type of Finite Elements and Steps in. *Machine Design*, 54–58.

[29] Cook, R. D., D. S. Malkus, M. E. Plesha, and R. J. Witt (2007). *Concept and Applications of Finite Element Analysis*. New York, NY: John Wiley & Sons.

[30] Autodesk Knowledge (2015). How to Perform and Mesh Convergence Study.

[31] Cresdee, R., W. Edwards, P. Thomas, and G. Voss (1992). Analysis of beam distortion during hot dip galvanizing. *Materials Science and Technology 9*(2), 161–162.

[32] Johnson, W. H. (1875). On some remarkable Changes Produced in Iron and Steel by the Action of Hydrogen and Acids. In *Proceedings of the Royal Society of London*, London, pp. 168. Taylor and Francis.

[33] Louthan, M. R. J. (2008). Hydrogen Embrittlement of Metals: A Primer for Failure Analyst.

[34] Kinstler, T. J. (2005). Current knowledge of the cracking of steels during galvanizing a synthesis of the available technical literature and collective experience.

[35] Marcelo, A. L., R. C. Tokimatsu, and I. Ferreira (2009). Hydrogen embrittlement in an AISI 1045 steel component of the sugarcane industry. *Engineering Failure Analysis 16*(1), 468–474.

[36] Yu, H., D. Zeng, and Z. Liu (2010). Failure analysis on the rivet. *Materials Science Forum 654-656*(June).

[37] lei Xu, X., Z. wei Yu, Z. Yang, and Y. zhen Chen (2011). Intergranular brittle cracking of truck diesel fuel filter-cases. *Engineering Failure Analysis 18*(8), 2054–2063.

[38] Brahimi Eng, S., S. Brahimi -, and S. Brahimi (2014). HYDROGEN EMBRITTLEMENT IN STEEL FASTENERS Fundamentals of hydrogen embrittlement in steel fasteners Fundamentals of hydrogen embrittlement in steel fasteners. pp. 1–23.

[39] Brahimi, S., S. Rajagopalan, S. Yue, and J. Szpunar (2009). Effect of Surface Processing Variables on Hydrogen Embrittlement of Steel Fasteners Part 1 : Hot Dip Galvanizing. *48*(3), 293–301.

[40] Recio, F. J., M. C. Alonso, L. Gaillet, and M. Sánchez (2011). Hydrogen embrittlement risk of high strength galvanized steel in contact with alkaline media. *Corrosion Science 53*(9), 2853–2860.

[41] ASTM Internatinal (2017). Standard Test Methods and Definitions for Mechanical Testing of Steel Products.

[42] Ding, R., A. Islam, S. Wu, and J. Knott (2005). Effect of phosphorus segregation on fracture properties of two quenched and tempered structural steels. *Materials Science and Technology 21*(4), 467–475.

[43] Christien, F., R. Le Gall, and G. Saindrenan (2003). Phosphorus grain boundary segregation in steel 17-4 PH. *Scripta Materialia 48*(3), 301–306.

[44] Borges, D., V. D. Castro, J. M. Ventura, C. Olivio, F. Terra, S. Paulo, A. T. São-carlense, P. A. Schmidt, and S. Carlos (2010). Influence of Phosphorus Content and Quenching / Tempering Temperatures on Fracture Toughness and Fatigue Life of SAE 5160 Steel. *Materials Research 13*(4), 445–455.

[45] Matsuyama, T., H. Hosokawa, and H. Suto (1983). Tracer Diffusion of P in Iron and Iron Alloys. *Transactions of the Japan Institute of Metals 24*(8), 589–594.

[46] Beckhoff, B., B. Kanngieber, N. Langhoff, R. Wedell, and H. Wolff (2006). *Handbook of Practical X-Ray Fluorescence Analysis* (First ed.). Berlin: Springer.

[47] Shimadzu (2014). Principle of Optical Emission Spectrometry.

[48] CSA Group (2013). Standard G40.20/G40.21 General requirements for rolled or welded structural quality steel / Structural quality steel.

[49] Charles, B. and K. Fredeen (2004). *Concepts, Instrumentation and Techniques in Inductively Coupled Plasma Optical Emission Spectrometry* (3rd ed.). Perkin Elmer.

[50] Kung, K.-h. (1965). *A study of hot shortness in steels.* Ph. D. thesis, Missouri University of Science and Technology.

[51] Liu, Z., Y. Kobayashi, M. Kuwabara, and K. Nagai (2007). Interaction between Phosphorus Micro-Segregation and Sulfide Precipitation in Rapidly Solidified Steel Utilization of Impurity Elements in Scrap Steel. *48*(12), 3079–3087.

[52] Askeland, D., P. Fulay, and W. Wright (2011). *The Science and Engineering of Materials* (Sixth ed.). Stamford, CT: Cengage Learning.

Appendix A: Base Material and Weld Images

This appendix provides further microscope images of the base material from Chapter 2 and introduces images of the weld cross section, both macroscopically and microscopically.

A.1. Base Material Images

Higher and lower magnification images of the T-joint base material section, shown in Chapter 2, are given in Fig. A.1 and Fig. A.2.

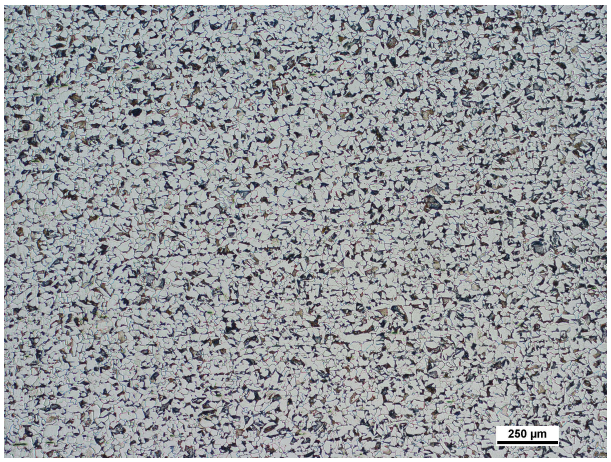

(a) Horizontal member at 5X

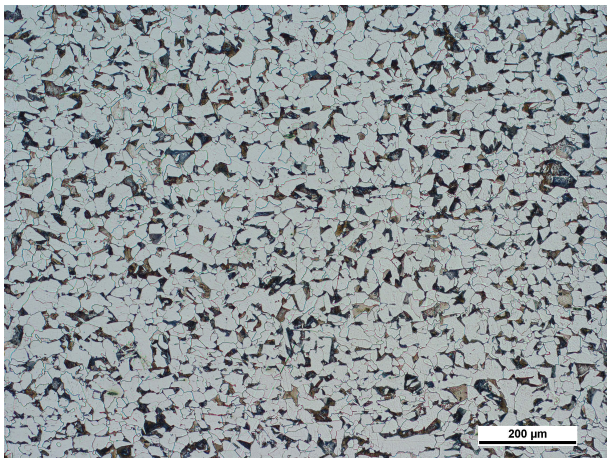

(b) Horizontal member at 10X

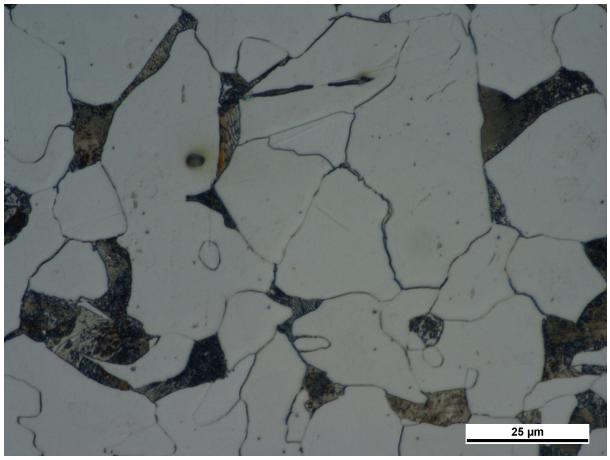

(c) Horizontal member at 100X

Fig. A.1: 5X, 10X and 100X of T-joint horizontal member's base material

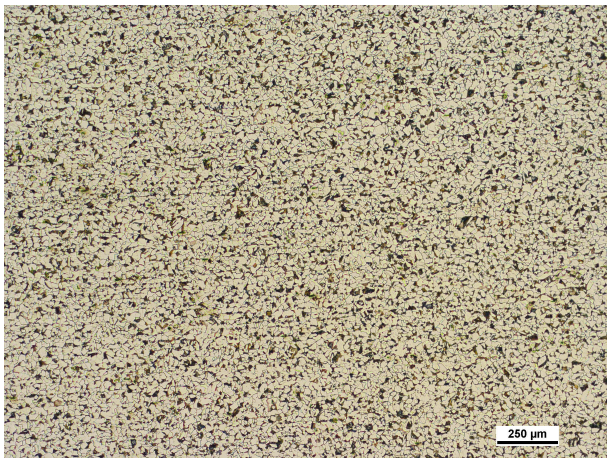

(a) Vertical member at 5X

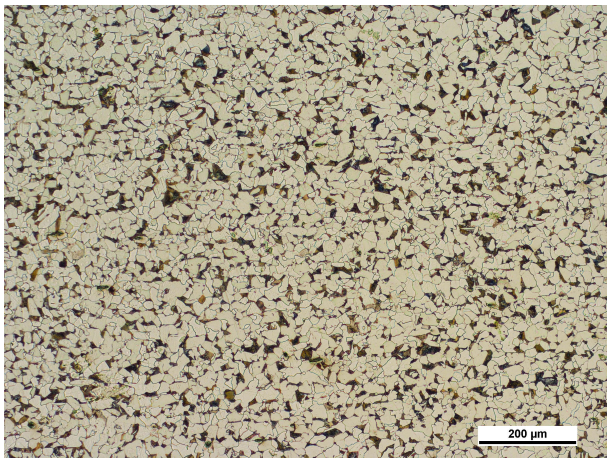

(b) Vertical member at 10X

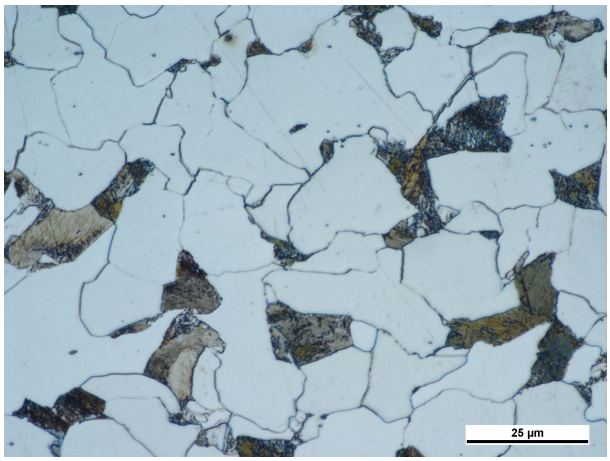

(c) Vertical member at 100X

Fig. A.2: 5X, 10X and 100X of T joint vertical member's base material

Another T-joint was sectioned and cut to prepare samples for further mechanical testing. However, base material samples were still taken from this T-joint for analysis. Images of the microstructure of the horizontal and vertical members are shown in Fig. A.3 and Fig. A.4. The features of the microstructure were similar to what shown in the previous base material samples in Chapter 2 and in Fig. A.1 and Fig. A.2.

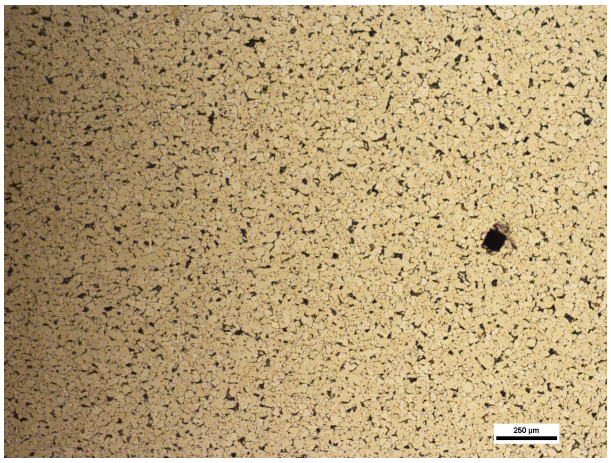

(a) Horizontal member at 5X

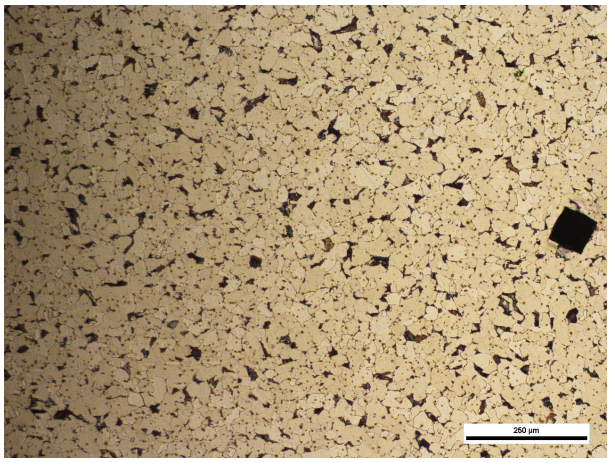

(b) Horizontal member at 10X

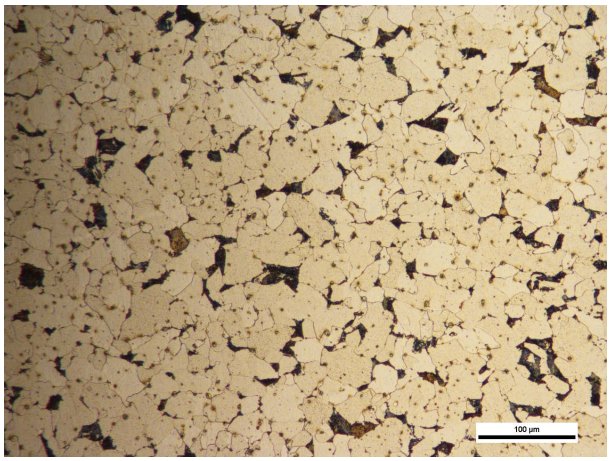

(c) Horizontal member at 100X

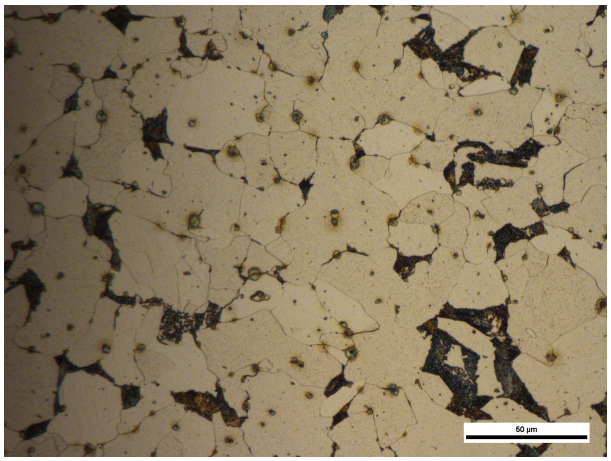

(d) Horizontal member at 50X

Fig. A.3: 5X, 10X and 100X of T-joint horizontal member's base material

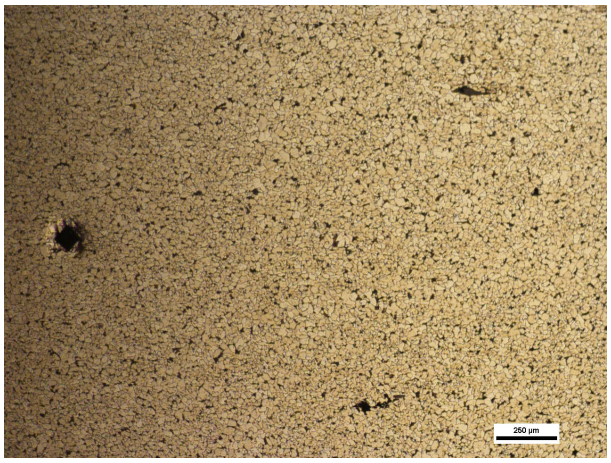

(a) Vertical member at 5X

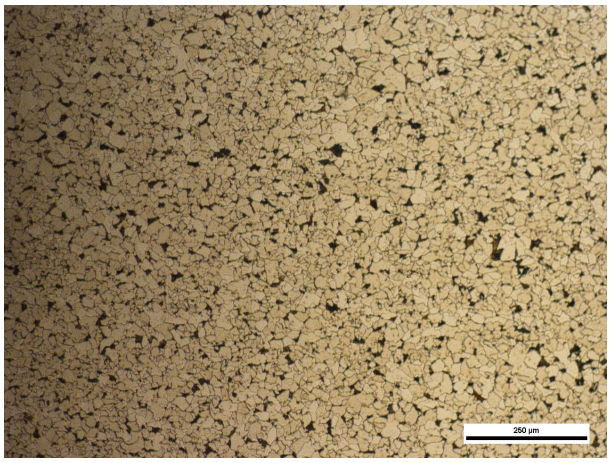

(b) Vertical member at 10X

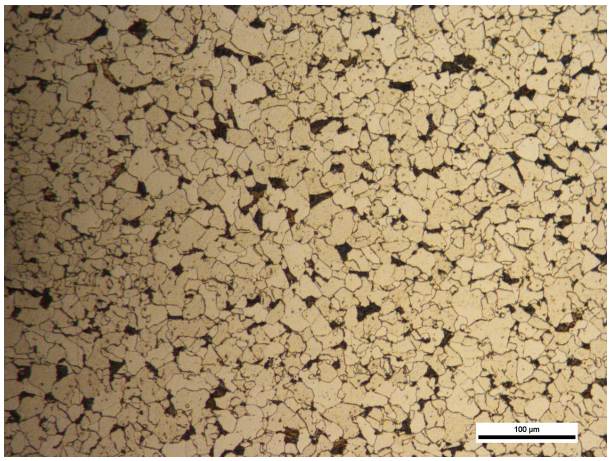

(c) Vertical member at 100X

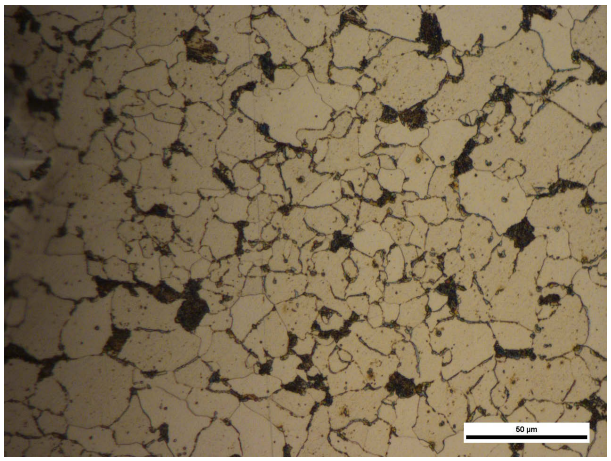

(d) Vertical member at 50X

Fig. A.4: 5X, 10X and 100X of T-joint vertical member's base material

A.2. Weld Images

The welded joints were also prepared and analyzed in the same fashion as the base material. The cross section of the welds was the surface of study, and images of the different cross sections can be seen in Fig. A.5.

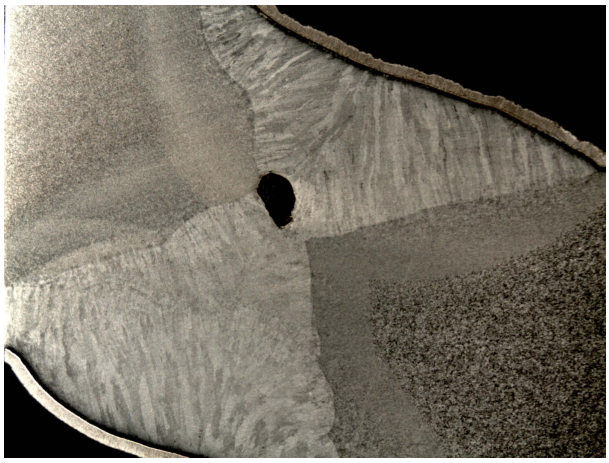

(a) Weld cross section of the corner joint

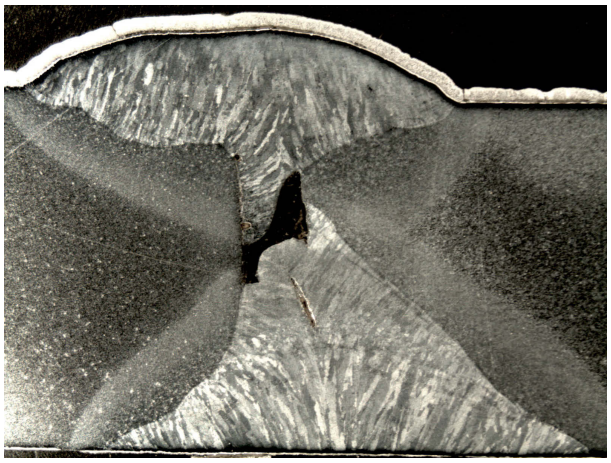

(b) Weld cross section of the T-joint, top flange

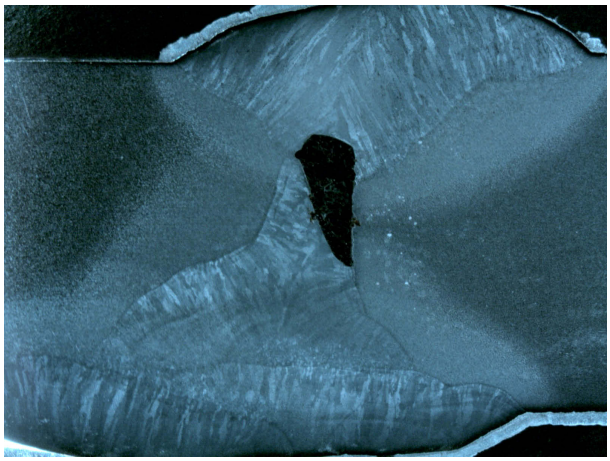

(c) Weld cross section of the T-joint, bottom flange

Fig. A.5: Different weld cross sections in the platform

Along with the optical microscope analysis of the base material, the weld cross section of the corner joint is shown in Fig. A.6. The images show the fusion zone, the fusion boundary, the heat affected zone, and heat affected zone boundary.

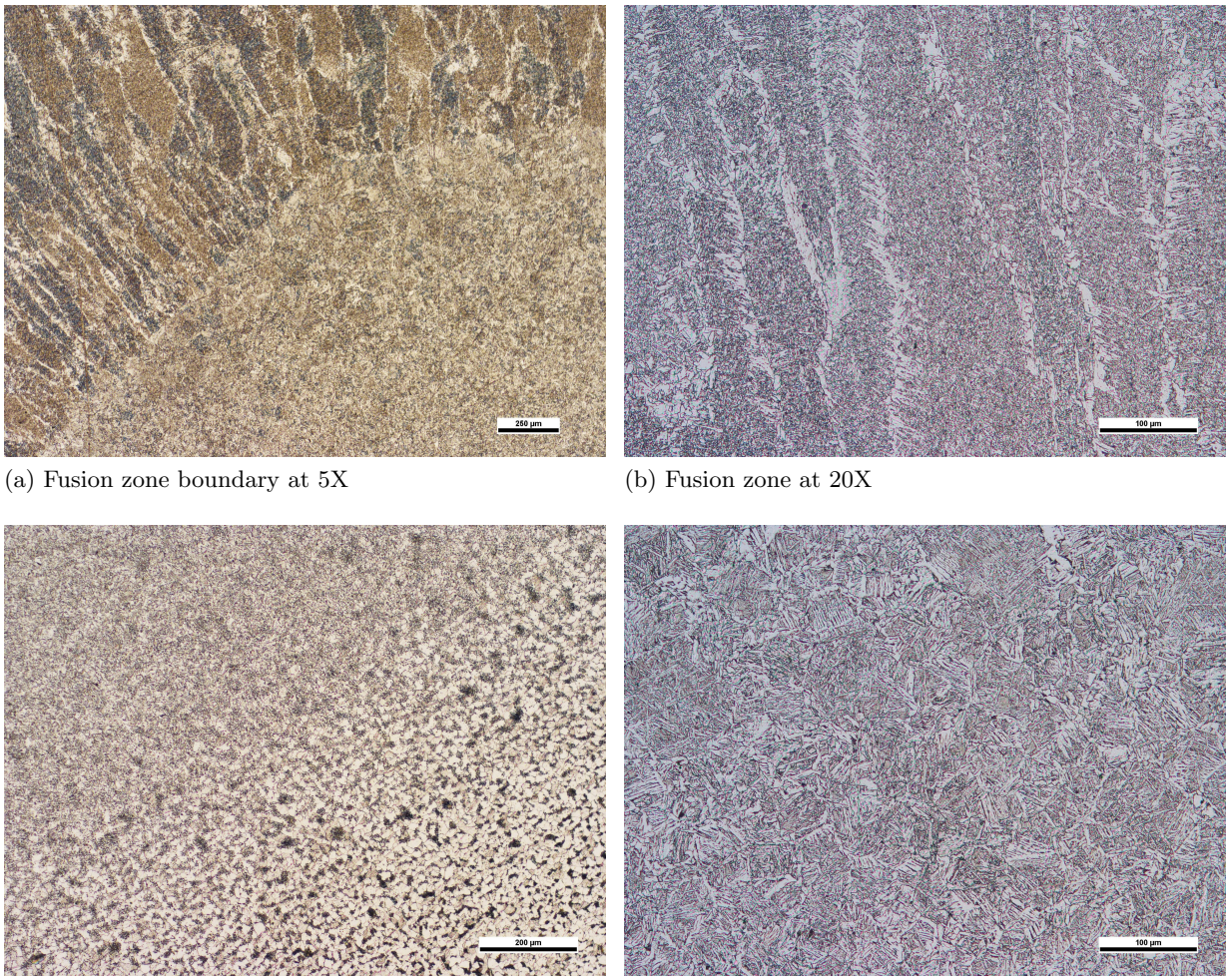

(a) Fusion zone boundary at 5X

(b) Fusion zone at 20X

(c) Heat affected zone boundary at 10X

(d) Heat affected zone at 20X

Fig. A.6: Fusion zone and heat affected zone of the corner joint's weld

Images of the side view of the weld were also captured at the crack initiation site. As an extension to the images in Fig. 2.10, lower magnification pictures are shown in Fig. A.7, Fig. A.8, and Fig. A.9.

Fig. A.7: Side view of the corner joint weld

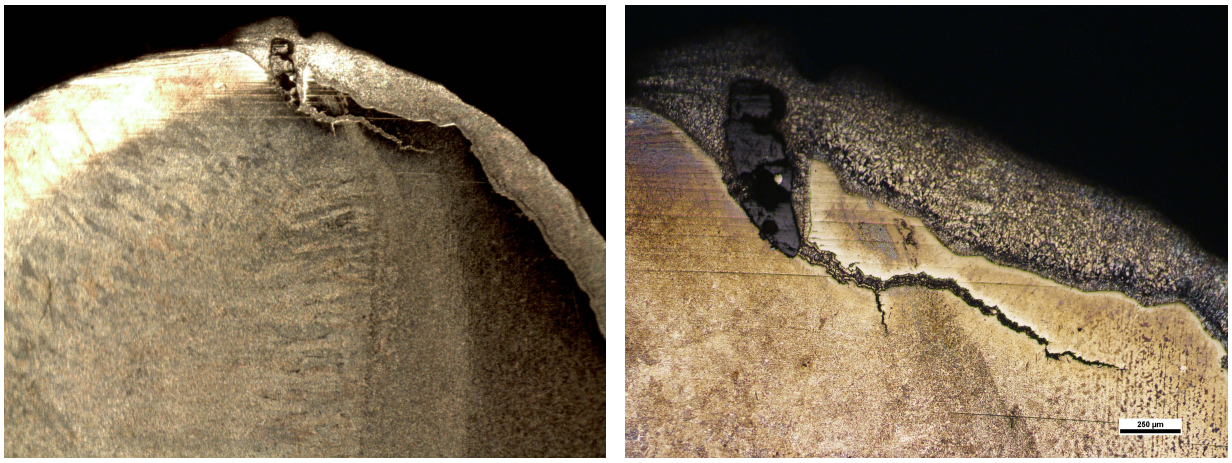

(a) Crack initiation site and upper secondary crack (b) 5X of upper secondary crack

Fig. A.8: Side view of the upper cracks in the corner joint weld

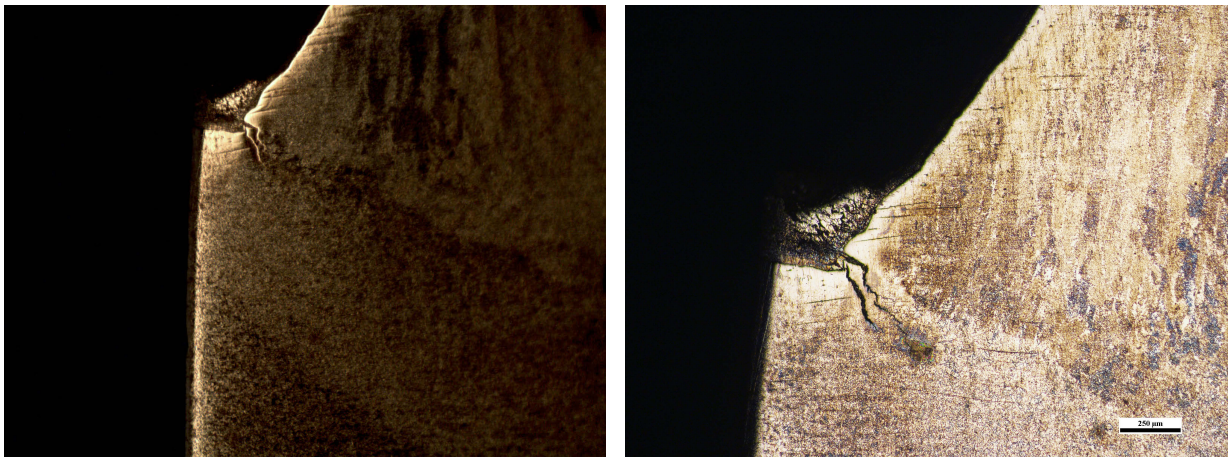

(a) Lower secondary crack (b) 5X of lower secondary crack

Fig. A.9: Side view of the lower cracks in the corner joint weld